Article | Received 26 February 2026; Revised 16 May 2026; Accepted 17 August 2026; Published 18 September 2026
https://doi.org/10.55092/aic20260013

A system-level simulation framework for performance evaluation of ultra-dense wireless networks

Thuan Van Le[1,*], Nam Van Dinh[2], Ngoc-Thanh Nguyen[1] and Nguyen Cong Luong[2]

[1] Faculty of Electrical and Electronic Engineering, Phenikaa School of Engineering, Phenikaa University, Hanoi, Vietnam

[2] Phenikaa School of Computing, Phenikaa University, Hanoi, Vietnam

* Correspondence author; E-mail: thuan.levan@phenikaa-uni.edu.vn.

Highlights:

- A unified receiver-aware SLS chain integrates beamforming, CSI errors, and EESM.
- 3GPP InH_B calibration verifies the system-level implementation and link abstraction.
- IRC yields 42% higher cell throughput and over 160% higher 5th-percentile UE throughput.

Abstract: Accurate evaluation of radio access performance is essential for the design and optimization of ultra-dense fifth-generation (5G) networks, where the interactions between multiple users, base stations, and interference sources become highly complex. This paper proposes a comprehensive System-Level Simulation (SLS) framework for assessing the performance of multi-user multiple-input multiple-output (MIMO) systems in indoor hotspot environments, following the standardized 3rd generation partnership project (3GPP) InH_B channel model. The proposed framework integrates realistic network-level processes, including user equipment deployment, three-dimensional channel coefficient generation, analog and digital beamforming, link adaptation, and block error rate prediction. Different from conventional SLS studies that often decouple receiver processing, channel state information (CSI) uncertainty, and link abstraction, the proposed framework provides a unified receiver-aware evaluation chain calibrated against 3GPP Phase 2 results. Both Maximal Ratio Combining (MRC) and Interference Rejection Combining (IRC) receivers are implemented to investigate the impact of imperfect CSI on system performance. Extensive simulations demonstrate that the proposed framework provides close agreement with the 3GPP Phase 2 calibration results, while enabling detailed receiver-level comparisons under practical CSI conditions. When CSI errors are considered, the IRC receiver achieves approximately 42% higher average cell throughput and more than 160% improvement in 5% user throughput compared to MRC, confirming its superior robustness to interference and channel estimation errors. The developed framework serves as a practical reference platform for future research on intelligent beamforming, adaptive MIMO receiver design, and machine learning-based link adaptation for beyond-5G and sixth-generation (6G) systems.

Keywords: ultra-dense network; system-level simulation; performance evaluation; indoor hotspot; eMBB; link adaptation

1. Introduction

The rapid growth of mobile data traffic and the stringent demands for high throughput, ultra-low latency, and massive connectivity in fifth-generation (5G) and beyond networks have driven the adoption of ultra-dense network (UDN) architectures [1–3]. In UDNs, a large number of small cells are densely deployed to shorten the transmission distance between base stations (BSs) and user equipments (UEs), thereby improving spectral efficiency and user experience [4,5]. By enabling aggressive spatial reuse, UDNs can potentially deliver multi-gigabit data rates and consistent service quality even in complex indoor environments. However, dense deployments also introduce strong inter-cell interference, irregular traffic load distributions, and sensitivity to channel estimation errors, which collectively make performance evaluation of UDNs a non-trivial task [6,7].

System-level simulation (SLS) tools have become indispensable for the design and optimization of dense cellular networks since they are able to jointly capture physical-layer behavior and network-level interactions [8,9]. Such simulations enable the study of user association, scheduling, beamforming, interference coordination, and throughput aggregation in large-scale scenarios. Existing SLS platforms, including Vienna 5G SLS, ns-3 with long-term evolution (LTE)/new radio (NR) modules, and several proprietary frameworks, typically trade accuracy for scalability by assuming idealized conditions—such as perfect channel state information (CSI), simplified antenna models, or neglecting link abstraction [10,11]. Consequently, there remains a gap between detailed link-level fidelity and full-scale network simulation capability. Recent efforts, such as SeBaSi [12] and simulators for Integrated Access and Backhaul (IAB) networks [13,14], have improved modularity and extensibility, but they rarely address realistic CSI imperfections or the combined effect of analog beamforming and receiver algorithms in ultra-dense topologies.

Another line of research focuses on robust and hybrid analog/digital precoding techniques under imperfect CSI conditions, particularly for massive multiple-input multiple-output (MIMO) and millimeter-wave systems. For example, sub-connected hybrid architectures with successive interference cancellation have been proposed to enhance energy efficiency [15], while probabilistic and learning-based approaches have been applied to symbol-level precoding to mitigate CSI uncertainty [16]. Although these approaches are promising, they typically focus on link-level analysis or small-scale multiuser MIMO systems and do not extend to large-scale UDN environments that involve complex interference coupling and heterogeneous deployments.

In ultra-dense indoor scenarios, the joint impact of analog beamforming, receiver interference suppression (e.g., Maximal Ratio Combining (MRC) [17,18] and Interference Rejection Combining (IRC) [19]), and CSI errors has not been systematically analyzed within a unified system-level evaluation platform. To bridge this gap, this paper develops a comprehensive SLS framework that integrates realistic 3rd generation partnership project (3GPP) channel modeling, BS–UE association, analog precoding, interference-aware receivers, and link abstraction using Exponential Effective SNR Mapping (EESM). The proposed framework is aligned with [20] and [21] recommendations, providing a balance between simulation accuracy and computational scalability. The novelty of this work lies in developing a calibrated receiver-aware SLS framework that jointly connects 3GPP InH_B channel generation, panel-based antenna modeling, discrete Fourier transform (DFT)/sounding reference signal (SRS)-based beam selection, CSI-error modeling, MRC/IRC receiver processing, dominant-interferer approximation, and EESM-based block error rate (BLER)/throughput prediction. This unified treatment distinguishes the proposed platform from conventional SLS tools that often simplify receiver processing or CSI uncertainty, and from link-level studies that do not capture dense multi-cell interference and network-level performance aggregation.

The main contributions of this paper are summarized as follows:

- We develop a modular receiver-aware SLS framework for ultra-dense indoor 5G MIMO networks, integrating 3GPP InH_B channel generation, panel-based antenna modeling, DFT-based analog precoding, SRS-assisted beam-pair selection, EESM-based link adaptation, and BLER-driven throughput evaluation into a unified simulation chain.
- We incorporate a practical CSI-error model and a dominant-interferer approximation into the SLS framework, enabling scalable yet realistic evaluation of interference-limited dense deployments. The framework explicitly captures the impact of CSI uncertainty on signal-to-interference-plus-noise ratio (SINR), spectral efficiency, BLER, and throughput.
- We provide a calibrated receiver-level comparison between MRC and IRC under both perfect and imperfect CSI conditions. The proposed simulator is validated against 3GPP Phase-2 calibration results and further used to quantify the robustness of IRC in terms of average throughput and 5% cell-edge user performance.

The remainder of this paper is organized as follows. Section 2 describes the architecture and modules of the proposed SLS platform. Section 3 presents the simulation setup and performance analysis under both perfect and imperfect CSI conditions. Finally, Section 4 concludes the paper and outlines future research directions toward intelligent beamforming and learning-assisted link adaptation for ultra-dense sixth-generation (6G) networks.

2. System model and simulation framework

This section describes the overall architecture and modeling flow of the proposed SLS platform developed for ultra-dense 5G networks. The proposed SLS framework is organized into a sequence of functional modules, each representing a specific stage of the end-to-end simulation chain. First, the overall network layout, antenna configuration, and deployment assumptions are introduced, together with the structural organization of the SLS platform (Sections 2.1, 2.2). Next, the initialization and run-time simulation phases are detailed to explain how the framework generates network topology, schedules simulation drops, and performs per-transmission time interval (TTI) processing (Sections 2.3, 2.4). After that, the UE placement, association with serving BSs, and large-scale propagation modeling, including distance computation, path loss, and line-of-sight (LoS) probability under the 3GPP InH_B scenario, are presented (Sections 2.5, 2.6). Subsequently, the small-scale fading model and channel-coefficient generation are described, followed by the analog precoding, SRS-based beam-pair selection, and receiver combining mechanisms (Sections 2.7–2.10). Finally, link adaptation, BLER estimation, and throughput computation are explained, forming the performance evaluation layer of the SLS simulation process (Sections 2.11, 2.12). This modular design ensures a clear separation between physical-layer modeling, beamforming, and link adaptation processes, facilitating scalable system-level evaluations for ultra-dense 5G and beyond-5G networks.

2.1. *Network layout*

The simulation adopts the Indoor Hotspot enhanced Mobile Broadband (eMBB) environment, corresponding to Configuration B in [20]. The layout consists of a single floor of a building with a height of 3 m and an area of 120 m × 50 m. A total of 12 BSs sites are uniformly deployed with an inter-site distance of 20 m, as illustrated in Figure 1. Each BS is equipped with N_{BS} antenna ports following a panel-based antenna configuration, as illustrated in Figure 2.

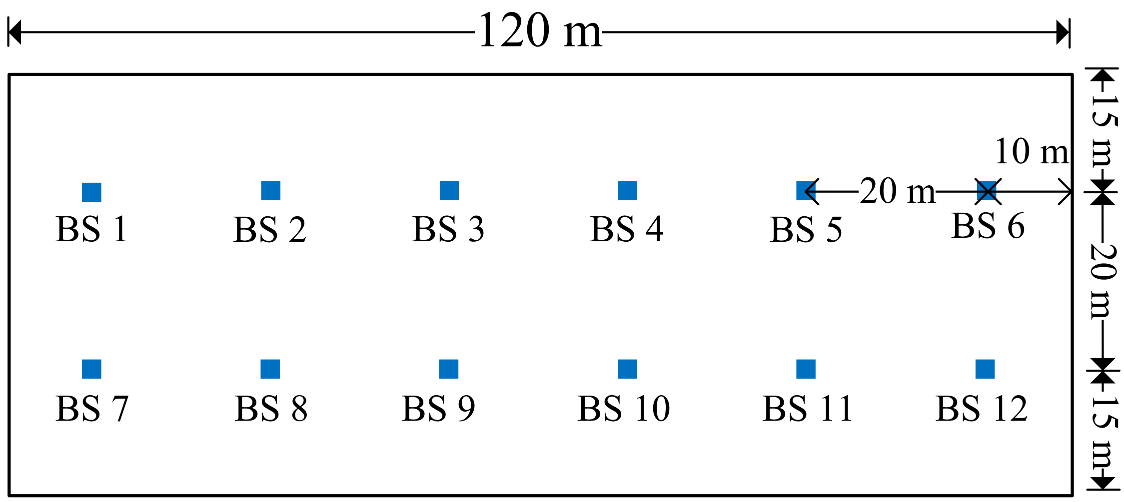

Figure 1. Indoor Hotspot-eMBB network layout: a single-floor building (120 m × 50 m) with 12 BS sites spaced by 20 m.

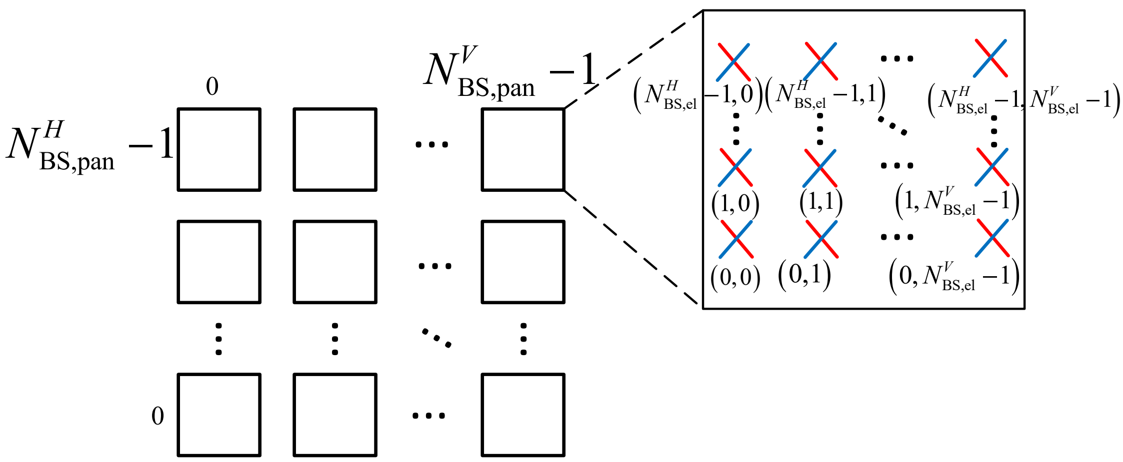

Figure 2. Panel-based antenna configuration. For node $q \in \{\mathrm{BS}, \mathrm{UE}\}$, the array contains $N^{\mathrm{H}}_{q,\mathrm{pan}} \times N^{\mathrm{V}}_{q,\mathrm{pan}}$ panels, and each panel consists of $N^{\mathrm{H}}_{q,\mathrm{el}} \times N^{\mathrm{V}}_{q,\mathrm{el}}$ antenna elements. Each element supports P_q polarization ports, resulting in $N_q = N^{\mathrm{H}}_{q,\mathrm{pan}} N^{\mathrm{V}}_{q,\mathrm{pan}} N^{\mathrm{H}}_{q,\mathrm{el}} N^{\mathrm{V}}_{q,\mathrm{el}} P_q$ antenna ports.

For compact notation, let $q \in \{\mathrm{BS}, \mathrm{UE}\}$ denote either the BS or UE side. The antenna array of node q consists of $N_{q,\mathrm{pan}}^{\mathrm{H}} \times N_{q,\mathrm{pan}}^{\mathrm{V}}$ panels arranged in the horizontal and vertical directions, respectively. Each panel contains $N_{q,\mathrm{el}}^{\mathrm{H}} \times N_{q,\mathrm{el}}^{\mathrm{V}}$ antenna elements, where $N_{q,\mathrm{el}}^{\mathrm{H}}$ and $N_{q,\mathrm{el}}^{\mathrm{V}}$ denote the numbers of elements per panel in the horizontal and vertical dimensions, respectively. Each antenna element supports P_q polarization ports. Therefore, the total number of antenna ports at node q is

$$N_q = N_{q,\mathrm{pan}}^{\mathrm{H}} N_{q,\mathrm{pan}}^{\mathrm{V}} N_{q,\mathrm{el}}^{\mathrm{H}} N_{q,\mathrm{el}}^{\mathrm{V}} P_q. \tag{1}$$

Accordingly, N_{BS} and N_{UE} denote the total numbers of antenna ports at the BS and UE, respectively. A total of 120 UEs are uniformly distributed over the simulation floor area.

Internal walls are not geometrically modeled. Instead, the LoS probability of each BS–UE pair is determined stochastically using the indoor channel formulation provided in [20]. This probabilistic LoS model effectively captures the shadowing and obstruction characteristics of typical indoor office environments. The network operates without wrap-around boundaries, and the heights of BS and UE antennas are denoted as h_{BS} and h_{UE}, respectively.

2.2. SLS structure

The overall operation of the proposed SLS platform is organized into three main stages: parameter configuration, initialization, and simulation and performance evaluation. At the beginning of each simulation run, the parameter configuration block loads all system parameters, including carrier frequency, bandwidth, number of BSs and UEs, antenna settings, and channel models. After configuration, the simulator executes a series of independent drops, each corresponding to a different random deployment of UEs within the specified environment.

For each drop, the initialization phase configures the channel conditions and network associations. The following steps are performed sequentially:

(1) Generate large-scale and small-scale parameters between every UE–BS pair.

(2) Assign each UE to the BS providing the maximum reference signal received power (RSRP).

(3) Select an optimal DFT-based beam pair that maximizes the received signal power.

(4) Enable either MRC or IRC with optional CSI error modeling.

The simulation phase then iterates over multiple TTIs. For each TTI, scheduling, transmission, and channel updates are executed. The SINR, spectral efficiency, and BLER are computed using EESM to approximate link-level behavior. After completing all TTIs, throughput and user statistics are collected to derive the cumulative distribution functions (CDFs) of SINR and spectral efficiency (SE).

2.3. Initialization phase

The initialization phase prepares the simulation environment before each network realization (drop). Its main purpose is to configure user positions, establish channel parameters, and compute the propagation coefficients between all UEs and BSs. The process involves the following functional blocks:

(1) Randomly generate the spatial locations of UEs within the simulation area using Algorithm 1. Each UE is associated with the BS that provides the maximum RSRP.

(2) Initialize all propagation links between BSs and UEs, including antenna configurations, carrier

frequency f_c, and channel bandwidth B.

(3) Compute and assign large-scale parameters such as path-loss, shadow fading, delay spread, and angle spreads according to the channel model in [20].

(4) Generate small-scale parameters, including multipath components, cluster powers P_n, and delays based on the stochastic channel realization.

(5) Combine large-scale and small-scale components to compute the complete complex channel coefficient matrix $\mathbf{H}_{n,i}[k,t]$ for each UE i and BS n in subcarrier frequency f_k and time slot t.

The output of this phase is a fully parameterized channel model that captures both large-scale and small-scale fading characteristics, enabling realistic evaluation of multi-cell interference and spatial correlation effects. The resulting coefficients are then used in the subsequent simulation phase for analog precoding, signal reception, and performance evaluation.

Algorithm 1 UE Drop and UE–BS Association

Input: $\text{UE}_0, \dots, \text{UE}_{119}$, $\text{BS}_0, \dots, \text{BS}_{11}$

$i_{\text{MS}} \leftarrow 0$;
$n_i \leftarrow 0,\ i = 1, \dots, 12$;
while $i_{\text{MS}} < 120$ **do**
  Randomly drop $\text{UE}_{i_{\text{MS}}}$ on the simulation floor;
  for $i_{\text{BS}} \leftarrow 1$ **to** 12 **do**
    Compute distance $d_{i_{\text{BS}}, i_{\text{MS}}}$;
    Compute PL and SL using the large-scale model;
    Compute antenna gains G_n and G_i;
    Evaluate $\text{RSRP}_{i_{\text{BS}}}$ using Equation (4);
  end
  $i^*_{\text{BS}} \leftarrow \arg\max_i \text{RSRP}_i$;
  if $n_{i^*_{\text{BS}}} < 10$ **then**
    Assign $\text{UE}_{i_{\text{MS}}}$ to $\text{BS}_{i^*_{\text{BS}}}$;
    $n_{i^*_{\text{BS}}} \leftarrow n_{i^*_{\text{BS}}} + 1$;
    $i_{\text{MS}} \leftarrow i_{\text{MS}} + 1$;
  end
end

2.4. Simulation phase

The simulation phase models the dynamic transmission and reception process across multiple TTIs. It executes sequentially after the initialization phase to capture temporal channel evolution, resource allocation, and signal processing at both transmitter and receiver ends. The phase consists of the following key modules:

(1) Update the MIMO channel coefficients over time according to user mobility and small-scale fading dynamics. Temporal correlation is modeled using the Doppler spectrum associated with the carrier frequency.

(2) Allocate radio resources to users using a Round-Robin scheduler [22]. The modular structure allows easy replacement with proportional-fair [23,24] or channel quality indicator (CQI)-based schedulers [25] for future studies.

(3) Perform downlink (DL) beam selection using a DFT-based analog precoder [26]. The beam pair that maximizes the received signal power is selected among the predefined codebook.

(4) Each UE applies receive beamforming and combines signals using either MRC or IRC. CSI errors are modeled as additive perturbations to the estimated channel matrices.

(5) Compute key performance indicators such as instantaneous SINR, throughput, and spectral efficiency (SE) at every TTI.

To reduce computational complexity while preserving the dominant spatial interference structure, the proposed SLS platform explicitly generates small-scale MIMO channels only for the four strongest interfering BSs of each scheduled UE. These interferers are selected according to their large-scale received powers, including path loss, shadowing, and antenna gains. The remaining interfering BSs are represented by their average large-scale interference powers. This hybrid approach is commonly adopted in 3GPP-style link-to-system evaluations, where dominant interferers are modeled explicitly and weak residual interference is statistically averaged. It is effective because the strongest few interferers dominate the instantaneous interference covariance and post-combining SINR, whereas far or weak interferers mainly contribute to the average interference floor over multiple drops and TTIs.

Let $\mathscr{D}_i(t)$ denote the set of dominant interfering BSs for UE i at TTI t, with $|\mathscr{D}_i(t)| = 4$. The total interference power on resource block (RB) r is then approximated as

$$I_{i,r}[t] = \sum_{m \in \mathscr{D}_i(t)} P_m \left| \mathbf{w}_i^H \mathbf{H}_{m,i}[r,t] \mathbf{f}_m \right|^2 + \sum_{m \notin \mathscr{D}_i(t), m \neq n_i^\star} \bar{I}_{m,i}, \tag{2}$$

where $n_i^\star$ is the serving BS of UE i, P_m is the transmit power of interfering BS m, and $\bar{I}_{m,i}$ denotes the average large-scale interference power from BS m to UE i. The first term captures instantaneous small-scale interference from the dominant interferers, while the second term accounts for the residual interference contributed by weaker cells.

The residual large-scale interference term is computed as

$$\bar{I}_{m,i} = P_m G_m G_i 10^{-\mathrm{PL}_{m,i}/10}, \tag{3}$$

where G_m and G_i are the corresponding BS and UE antenna gains, and $\mathrm{PL}_{m,i}$ includes path loss and shadow fading.

2.5. UE drop and UE–BS association

In each simulation drop, UEs are randomly distributed within the simulation area, and each UE is associated with the BS that provides the maximum RSRP. This procedure determines the cell assignment under large-scale channel conditions and ensures realistic load balancing among BSs. The process is summarized in Algorithm 1. The RSRP achieved by UE i when associated with BS n is computed as

$$\mathrm{RSRP}_{n,i} = P_n + G_n + G_i - \mathrm{PL}_{n,i}, \tag{4}$$

where P_n is the transmit power of BS n, G_n and G_i are the BS and UE antenna gains, and $\mathrm{PL}_{n,i}$ denotes the total path-loss including log-normal shadow fading. We denote n_i^* as the index representing UE i associated with BS n with maximum RSRP. Then, n_i^* is determined as follows:

$$n_i^* = \arg \max_{n \in \{1,\ldots,12\}} \mathrm{RSRP}_{n,i}. \tag{5}$$

The UE–BS association is stored for subsequent small-scale channel generation and link-level simulation.

2.6. Large-scale modeling: distance, path-loss, and LoS probability (InH_B)

Figure 3 shows the three-dimensional (3D) distance for each BS–UE pair (n,i), which is determined according to the InH definition as follows:

$$d_{\mathrm{3D}}^{(n,i)} = d_{\mathrm{3D\text{-}out}}^{(n,i)} + d_{\mathrm{3D\text{-}in}}^{(n,i)} = \sqrt{\left(d_{\mathrm{2D\text{-}out}}^{(n,i)} + d_{\mathrm{2D\text{-}in}}^{(n,i)}\right)^2 + \left(h_{\mathrm{BS}} - h_{\mathrm{UE}}\right)^2}. \tag{6}$$

Here, $d_{\mathrm{2D\text{-}out}}$ and $d_{\mathrm{2D\text{-}in}}$ denote the horizontal outdoor and indoor traversed distances, respectively, while h_{BS} and h_{UE} are the BS and UE antenna heights, respectively.

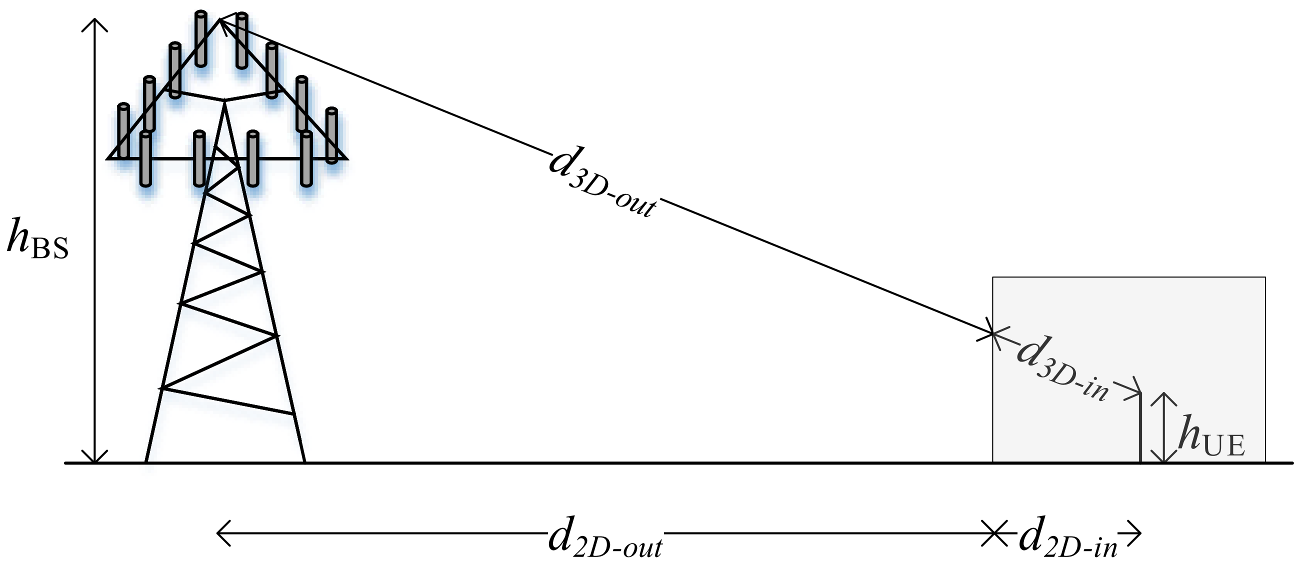

Figure 3. Geometry of the indoor hotspot (InH_B) link showing outdoor and indoor 2D components and antenna heights of BS and UE.

The large-scale path-loss for the Indoor Hotspot Configuration B (denoted InH_B) is evaluated for both LoS and non-line-of-sight (NLoS), which are expressed as follows:

$$\mathrm{PL}_{\mathrm{LoS}}^{(n,i)}(f_c, d_{\mathrm{3D}}) = \mathrm{FSPL}(f_c, 1\,\mathrm{m}) + 10\, n_{\mathrm{LoS}}^{\mathrm{InH\_B}} \log_{10}\left(d_{\mathrm{3D}}^{(n,i)}\right) + \chi_{\sigma,\mathrm{LoS}}^{\mathrm{InH\_B}}, \tag{7}$$

$$\mathrm{PL}_{\mathrm{NLoS}}^{(n,i)}(f_c, d_{\mathrm{3D}}) = \mathrm{FSPL}(f_c, 1\,\mathrm{m}) + 10\, n_{\mathrm{NLoS}}^{\mathrm{InH\_B}} \log_{10}\left(d_{\mathrm{3D}}^{(n,i)}\right) + \Delta_{\mathrm{NLoS}}^{\mathrm{InH\_B}} + \chi_{\sigma,\mathrm{NLoS}}^{\mathrm{InH\_B}}, \tag{8}$$

where $\mathrm{FSPL}(f_c, 1\,\mathrm{m}) = 32.4 + 20\log_{10}(f_c)$ is the free-space loss at 1 m, f_c is the carrier frequency in GHz, $n_{\mathrm{LoS/NLoS}}^{\mathrm{InH\_B}}$ are the environment-dependent path-loss exponents, $\Delta_{\mathrm{NLoS}}^{\mathrm{InH\_B}}$ is the NLoS offset, and $\chi_{\sigma,\cdot}^{\mathrm{InH\_B}} \sim \mathcal{N}(0, (\sigma_{\cdot}^{\mathrm{InH\_B}})^2)$ captures log-normal shadow fading of either LoS or NLoS path.

For the Indoor Hotspot (InH_x) channel model, the probability that a link between BS n and UE i is LoS depends on the two-dimensional distance $d_{\mathrm{2D}}^{(n,i)}$ between them. According to [20], the LoS probability is expressed as

$$p_{\text{LoS}}^{\text{InH}}(d_{2\text{D}}) = \begin{cases} 1, d_{2\text{D}} \leq 5 \text{ m}, \\ \exp\left(-\dfrac{d_{2\text{D}}-5}{70.8}\right), 5 \text{ m} < d_{2\text{D}} \leq 49 \text{ m}, \\ 0.54 \times \exp\left(-\dfrac{d_{2\text{D}}-49}{211.7}\right), d_{2\text{D}} > 49 \text{ m}. \end{cases} \tag{9}$$

This piecewise exponential model captures the transition from full LoS conditions at short distances to probabilistic LoS for longer separations typical indoor environments. For each BS–UE pair, a random Bernoulli trial with success probability $p_{\text{LoS}}^{\text{InH}}(d_{2\text{D}})$ determines whether the link follows the LoS or NLoS path-loss model described in Equations (7) and (8). The resulting large-scale attenuation is then expressed compactly as

$$\text{PL}_{n,i} = \begin{cases} \text{PL}_{\text{LoS}}^{(n,i)}(f_c, d_{3\text{D}}^{(n,i)}), & \text{if LoS}, \\ \text{PL}_{\text{NLoS}}^{(n,i)}(f_c, d_{3\text{D}}^{(n,i)}), & \text{if NLoS}. \end{cases} \tag{10}$$

2.7. *Channel-coefficient generation*

Each channel realization between BS n and UE i is represented by the complex MIMO channel matrix

$$\mathbf{H}_{n,i}[k,t] \in \mathbb{C}^{N_{\text{UE}} \times N_{\text{BS}}}, \tag{11}$$

where N_{BS} and N_{UE} denote the total numbers of antenna ports at the BS and UE, respectively, as defined in Equation (1). The channel matrix is constructed as the superposition of L scattering clusters, each containing N_ℓ sub-rays. Let $u \in \{1, \dots, N_{\text{BS}}\}$ and $s \in \{1, \dots, N_{\text{UE}}\}$ denote the BS-side transmit antenna-port index and the UE-side receive antenna-port index, respectively.

2.7.1. Cluster mean angles and sub-ray offsets

Let $\ell \in \{1, \dots, L\}$ denote the scattering clusters generated within each BS–UE link (n,i) at the channel level. Each cluster ℓ is composed of N_ℓ sub-rays indexed by $r \in \{1, \dots, N_\ell\}$, which represent small angular variations around the cluster's mean direction. For cluster ℓ, the mean azimuth and zenith angles of departure and arrival are denoted by AOD_ℓ, AOA_ℓ, ZOD_ℓ, and ZOA_ℓ. These quantities represent the central angles of the cluster relative to the BS and UE antenna boresights and are drawn from distributions defined by the angular spreads of σ_{ASD}, σ_{ASA}, σ_{ZSD}, and σ_{ZSA}. Then, we have $\text{AOD}_\ell \sim \mathscr{U}(0, 2\pi)$, $\text{AOA}_\ell \sim \mathscr{U}(0, 2\pi)$, $\text{ZOD}_\ell \sim \mathscr{N}(\pi/4, (\sigma_{\text{ZSD}})^2)$, and $\text{ZOA}_\ell \sim \mathscr{N}(\pi/4, (\sigma_{\text{ZSA}})^2)$.

The azimuth and elevation angles of each sub-ray (ℓ, r) are determined by

$$\phi_{\ell,r}^{\text{AOD}} = \text{AOD}_\ell + \sigma_{\text{ASD}} \Delta\theta_{\ell,r}, \tag{12}$$

$$\phi_{\ell,r}^{\text{AOA}} = \text{AOA}_\ell + \sigma_{\text{ASA}} \Delta\theta_{\ell,r}, \tag{13}$$

$$\theta_{\ell,r}^{\text{ZOD}} = \text{ZOD}_\ell + \tfrac{3}{8}\, 10^{\mu_{\text{ZSD}}} \Delta\theta_{\ell,r}, \tag{14}$$

$$\theta_{\ell,r}^{\text{ZOA}} = \text{ZOA}_\ell + \sigma_{\text{ZSA}} \Delta\theta_{\ell,r}, \tag{15}$$

where $\mu_{\text{ZSD}} = \log_{10}(\sigma_{\text{ZSD}})$ and $\Delta\theta_{\ell,r}$ are per–sub-ray offsets.

2.7.2. Direction vectors and array responses

The unit direction vectors in the global coordinate system (GCS) are

$$\mathbf{r}_{\mathrm{BS}}(\ell,r)=\begin{bmatrix}\sin\theta_{\ell,r}^{\mathrm{ZOD}}\cos\phi_{\ell,r}^{\mathrm{AOD}}\\ \sin\theta_{\ell,r}^{\mathrm{ZOD}}\sin\phi_{\ell,r}^{\mathrm{AOD}}\\ \cos\theta_{\ell,r}^{\mathrm{ZOD}}\end{bmatrix},$$

$$\mathbf{r}_{\mathrm{UE}}(\ell,r)=\begin{bmatrix}\sin\theta_{\ell,r}^{\mathrm{ZOA}}\cos\phi_{\ell,r}^{\mathrm{AOA}}\\ \sin\theta_{\ell,r}^{\mathrm{ZOA}}\sin\phi_{\ell,r}^{\mathrm{AOA}}\\ \cos\theta_{\ell,r}^{\mathrm{ZOA}}\end{bmatrix}. \tag{16}$$

Let λ denote the carrier wavelength. For a uniform planar array (UPA) architecture, the transmit and receive arrays are defined on a rectangular grid along the x– and y–axes with inter-element spacing $d=\lambda/2$. For the spatial array geometry, we define the effective horizontal and vertical spatial dimensions of node q as

$$N_q^{\mathrm{H}}=N_{q,\mathrm{pan}}^{\mathrm{H}}N_{q,\mathrm{el}}^{\mathrm{H}}, \qquad N_q^{\mathrm{V}}=N_{q,\mathrm{pan}}^{\mathrm{V}}N_{q,\mathrm{el}}^{\mathrm{V}}, \tag{17}$$

where $q\in\{\mathrm{BS},\mathrm{UE}\}$. Thus, N_q^{H} and N_q^{V} represent the total numbers of spatial antenna locations along the horizontal and vertical dimensions, respectively, excluding polarization duplication. The total number of antenna ports is then $N_q=P_qN_q^{\mathrm{H}}N_q^{\mathrm{V}}$. The element-position matrices $\mathbf{W}_{\mathrm{BS}}\in\mathbb{R}^{3\times N_{\mathrm{BS}}}$ and $\mathbf{W}_{\mathrm{UE}}\in\mathbb{R}^{3\times N_{\mathrm{UE}}}$ contain the Cartesian coordinates of the antenna ports. For dual-polarized elements, two polarization ports share the same spatial location but are treated as separate antenna ports in the MIMO channel matrix.

The array steering (response) vectors are defined as

$$\mathbf{a}_{\mathrm{BS}}(\ell,r)=\exp\left(j\tfrac{2\pi}{\lambda}\mathbf{W}_{\mathrm{BS}}^{\top}\mathbf{r}_{\mathrm{BS}}(\ell,r)\right), \tag{18}$$

$$\mathbf{a}_{\mathrm{UE}}(\ell,r)=\exp\left(j\tfrac{2\pi}{\lambda}\mathbf{W}_{\mathrm{UE}}^{\top}\mathbf{r}_{\mathrm{UE}}(\ell,r)\right), \tag{19}$$

where $\mathbf{r}_{\mathrm{BS}}(\ell,r)$ and $\mathbf{r}_{\mathrm{UE}}(\ell,r)$ are the unit direction vectors of sub-ray (ℓ,r) defined in Equation (16). Each element of $\mathbf{a}_{\mathrm{BS}}(\ell,r)$ or $\mathbf{a}_{\mathrm{UE}}(\ell,r)$ represents the relative phase across the array due to the arriving (or departing) wavefront at direction (ϕ,θ). Let (m,n) and (p,q) denote the horizontal and vertical indices of antenna elements on the BS and UE grids, respectively. Each column of $\mathbf{W}_{\mathrm{BS}}$ (or $\mathbf{W}_{\mathrm{UE}}$) specifies the (x,y,z) coordinates of a single antenna element relative to the array reference point, expressed in meters. The three-dimensional element-location matrices are then defined as

$$\mathbf{W}_{\mathrm{BS}}=\begin{bmatrix}x_{1,1} & x_{2,1} & \cdots & x_{N_{\mathrm{BS}}^{\mathrm{H}},N_{\mathrm{BS}}^{\mathrm{V}}}\\ y_{1,1} & y_{2,1} & \cdots & y_{N_{\mathrm{BS}}^{\mathrm{H}},N_{\mathrm{BS}}^{\mathrm{V}}}\\ z_{1,1} & z_{2,1} & \cdots & z_{N_{\mathrm{BS}}^{\mathrm{H}},N_{\mathrm{BS}}^{\mathrm{V}}}\end{bmatrix}=[md,nd,0]^T_{(m,n)\in[0,N_{\mathrm{BS}}^{\mathrm{H}}-1]\times[0,N_{\mathrm{BS}}^{\mathrm{V}}-1]}, \tag{20}$$

$$\mathbf{W}_{\mathrm{UE}}=\begin{bmatrix}x_{1,1} & x_{2,1} & \cdots & x_{N_{\mathrm{UE}}^{\mathrm{H}},N_{\mathrm{UE}}^{\mathrm{V}}}\\ y_{1,1} & y_{2,1} & \cdots & y_{N_{\mathrm{UE}}^{\mathrm{H}},N_{\mathrm{UE}}^{\mathrm{V}}}\\ z_{1,1} & z_{2,1} & \cdots & z_{N_{\mathrm{UE}}^{\mathrm{H}},N_{\mathrm{UE}}^{\mathrm{V}}}\end{bmatrix}=[pd,qd,0]^T_{(p,q)\in[0,N_{\mathrm{UE}}^{\mathrm{H}}-1]\times[0,N_{\mathrm{UE}}^{\mathrm{V}}-1]}. \tag{21}$$

The per-element complex gain between transmitter element u and receiver element s is

$$g_{s,u}(\ell,r) = \mathbf{a}_{\mathrm{UE}}(\ell,r)_s \mathbf{a}_{\mathrm{BS}}(\ell,r)_u^*. \tag{22}$$

2.7.3. Antenna patterns and polarization

For InH_B, ceiling-mounted BS and UE antenna patterns are used, each clipped at 25 dB. The vertical and horizontal pattern attenuations (in dB) are

$$F_{\mathrm{BS},v}^{\mathrm{dB}}(\ell,r) = -\min\left\{12\left(\frac{\theta_{\ell,r}^{\mathrm{ZOD}}-180^\circ}{90^\circ}\right)^2, 25\right\}, \tag{23}$$

$$F_{\mathrm{BS},h}^{\mathrm{dB}}(\ell,r) = -\min\left\{12\left(\frac{\phi_{\ell,r}^{\mathrm{AOD}}}{90^\circ}\right)^2, 25\right\}, \tag{24}$$

$$F_{\mathrm{UE},v}^{\mathrm{dB}}(\ell,r) = -\min\left\{12\left(\frac{\theta_{\ell,r}^{\mathrm{ZOA}}-90^\circ}{90^\circ}\right)^2, 25\right\}, \tag{25}$$

$$F_{\mathrm{UE},h}^{\mathrm{dB}}(\ell,r) = -\min\left\{12\left(\frac{\phi_{\ell,r}^{\mathrm{AOA}}}{90^\circ}\right)^2, 25\right\}. \tag{26}$$

The corresponding polarization power terms are

$$G_{pq}(\ell,r) = 10^{-\frac{F_{\mathrm{UE},p}^{\mathrm{dB}}(\ell,r)+F_{\mathrm{BS},q}^{\mathrm{dB}}(\ell,r)}{10}}, \; p,q \in \{v,h\}. \tag{27}$$

The cross-polarization power ratio (XPR) defines the leakage between orthogonal polarization components and is drawn from $\mathcal{N}(9,3^2)$ dB. With independent random phases $\{\varphi_{vv},\varphi_{vh},\varphi_{hv},\varphi_{hh}\} \sim \mathcal{U}[0,2\pi)$, the per-ray polarization gain is

$$A(\ell,r) = G_{vv}e^{j\varphi_{vv}} + G_{hh}e^{j\varphi_{hh}} + \sqrt{\frac{1}{\mathrm{XPR}}}\left(G_{vh}e^{j\varphi_{vh}} + G_{hv}e^{j\varphi_{hv}}\right). \tag{28}$$

2.7.4. Doppler frequency

For each sub-ray (ℓ,r), the Doppler shift is

$$f_D(\ell,r) = \frac{\mathbf{r}_{\mathrm{UE}}^\top(\ell,r)\mathbf{v}}{\lambda}, \tag{29}$$

where

$$\mathbf{v} = [v\sin\theta^{\mathrm{ZOA}}\cos\phi^{\mathrm{AOA}},\; v\sin\theta^{\mathrm{ZOA}}\sin\phi^{\mathrm{AOA}},\; v\cos\theta^{\mathrm{ZOA}}]^\top. \tag{30}$$

2.7.5. Time-domain and frequency-domain channel coefficients

Let P_ℓ be the normalized cluster power and N_ℓ the number of sub-rays per cluster. The diffuse (NLoS) component between TX antenna u and RX antenna s is

$$h_{s,u}^{\mathrm{NLoS}}(\ell,t) = \sqrt{\frac{P_\ell}{N_\ell}} \sum_{r=1}^{N_\ell} A(\ell,r)\, g_{s,u}(\ell,r)\, e^{j2\pi f_D(\ell,r)t}. \tag{31}$$

For LoS links with Rician factor $K_{\mathrm{lin}} = 10^{K_{\mathrm{dB}}/10}$, the total power is divided between the specular and diffuse parts as $\sqrt{\frac{K_{\mathrm{lin}}}{K_{\mathrm{lin}}+1}}$ and $\sqrt{\frac{1}{K_{\mathrm{lin}}+1}}$, respectively. The LoS component (for $\ell = 0$) is

$$h_{s,u}^{\mathrm{LoS}}(0,t) = \sqrt{\frac{K_{\mathrm{lin}}}{K_{\mathrm{lin}}+1}} \left(G_{vv}(0) e^{j\varphi_{vv}} + G_{hh}(0) e^{j\varphi_{hh}} \right) \times g_{s,u}(0, \mathrm{LoS})\, e^{j2\pi f_D(0)t}, \tag{32}$$

where $G_{vv}(0)$, $G_{hh}(0)$, and $f_D(0)$ are polarization powers and the Doppler shift of the LoS path, respectively. Finally, the composite baseband channel impulse response and the per-subcarrier frequency-domain response are

$$h_{s,u}^{(n,i)}(t,\tau) = \sum_{\ell} \left(\sqrt{\frac{1}{K_{\mathrm{lin}}+1}}\, h_{s,u}^{\mathrm{NLoS}}(\ell,t) + \mathbf{1}_{\{\ell=0\}}\, h_{s,u}^{\mathrm{LoS}}(0,t) \right) \delta(\tau - \tau_\ell), \tag{33}$$

$$H_{s,u}^{(n,i)}[k,t] = \sum_{\ell} \left(\sqrt{\frac{1}{K_{\mathrm{lin}}+1}}\, h_{s,u}^{\mathrm{NLoS}}(\ell,t) + \mathbf{1}_{\{\ell=0\}}\, h_{s,u}^{\mathrm{LoS}}(0,t) \right) e^{-j2\pi f_k \tau_\ell}, \tag{34}$$

where τ_ℓ denotes the delay of cluster ℓ and f_k the subcarrier frequency. The complete MIMO channel matrix $\mathbf{H}_{n,i}[k,t]$ is then assembled by stacking $H_{s,u}^{(n,i)}[k,t]$ across all antenna elements.

2.8. Analog precoding generation

To reduce hardware complexity while maintaining high beamforming gain, the proposed SLS framework employs analog beamforming based on DFT codebooks. At each transmission time interval, the analog beam pair that maximizes the received signal power is selected from a predefined DFT beam set. This approach provides near-optimal directional gain with low computational cost, making it suitable for large-scale ultra-dense network evaluations.

2.8.1. DFT beamforming vectors

For the BS UPA, the horizontal and vertical spatial dimensions are $N_{\mathrm{BS}}^{\mathrm{H}}$ and $N_{\mathrm{BS}}^{\mathrm{V}}$, respectively. The vertical and horizontal DFT beamforming vectors are defined as

$$\mathbf{w}_{\mathrm{V}}(\theta_a) = \frac{1}{\sqrt{N_{\mathrm{BS}}^{\mathrm{V}}}} \left[1, e^{j\theta_a}, \ldots, e^{j(N_{\mathrm{BS}}^{\mathrm{V}}-1)\theta_a} \right]^T,$$

$$\theta_a = \frac{\pi}{N_{\mathrm{BS}}^{\mathrm{V}}} \left(a - \frac{1}{2} \right), \quad a = 1, \ldots, N_{\mathrm{BS}}^{\mathrm{V}}, \tag{35}$$

$$\mathbf{w}_{\mathrm{H}}(\psi_b) = \frac{1}{\sqrt{N_{\mathrm{BS}}^{\mathrm{H}}}} \left[1, e^{j\psi_b}, \ldots, e^{j(N_{\mathrm{BS}}^{\mathrm{H}}-1)\psi_b} \right]^T,$$

$$\psi_b = \frac{\pi}{N_{\mathrm{BS}}^{\mathrm{H}}} \left(b - \frac{1}{2} \right), \quad b = 1, \ldots, N_{\mathrm{BS}}^{\mathrm{H}}. \tag{36}$$

The two-dimensional DFT beam is then constructed as

$$\mathbf{w}_{\mathrm{DFT}}(\theta_a, \psi_b) = \mathbf{w}_{\mathrm{V}}(\theta_a) \otimes \mathbf{w}_{\mathrm{H}}(\psi_b), \tag{37}$$

where $\otimes$ denotes the Kronecker product. This structure forms a separable beam pattern across both azimuth and elevation directions.

2.8.2. DFT-based codebook construction

To avoid ambiguity between the number of antenna ports and the number of spatial beams, we construct the DFT codebooks using the spatial array dimensions defined in Equation (17). For node $q \in \{\mathrm{BS}, \mathrm{UE}\}$, let N_q^{H} and N_q^{V} denote the total numbers of spatial antenna locations in the horizontal and vertical dimensions, respectively, excluding polarization duplication. The number of DFT beam directions at node q is therefore

$$N_q^{\mathrm{beam}} = N_q^{\mathrm{H}} N_q^{\mathrm{V}}. \tag{38}$$

For each vertical index $a = 1, \dots, N_q^{\mathrm{V}}$ and horizontal index $b = 1, \dots, N_q^{\mathrm{H}}$, the one-dimensional DFT phase samples are defined as

$$\theta_{q,a} = \frac{\pi}{N_q^{\mathrm{V}}}\left(a - \frac{1}{2}\right), \ \psi_{q,b} = \frac{\pi}{N_q^{\mathrm{H}}}\left(b - \frac{1}{2}\right). \tag{39}$$

The corresponding vertical and horizontal steering vectors are

$$\mathbf{v}_q^{\mathrm{V}}(\theta_{q,a}) = \frac{1}{\sqrt{N_q^{\mathrm{V}}}}\left[1, e^{j\theta_{q,a}}, \dots, e^{j(N_q^{\mathrm{V}}-1)\theta_{q,a}}\right]^T, \tag{40}$$

$$\mathbf{v}_q^{\mathrm{H}}(\psi_{q,b}) = \frac{1}{\sqrt{N_q^{\mathrm{H}}}}\left[1, e^{j\psi_{q,b}}, \dots, e^{j(N_q^{\mathrm{H}}-1)\psi_{q,b}}\right]^T. \tag{41}$$

The two-dimensional spatial DFT beam is then obtained by the Kronecker product

$$\widetilde{\mathbf{c}}_q(a,b) = \mathbf{v}_q^{\mathrm{V}}(\theta_{q,a}) \otimes \mathbf{v}_q^{\mathrm{H}}(\psi_{q,b}), \tag{42}$$

where $\widetilde{\mathbf{c}}_q(a,b) \in \mathbb{C}^{N_q^{\mathrm{V}} N_q^{\mathrm{H}}}$ is the spatial beam vector before polarization expansion.

For dual-polarized arrays, the same spatial direction is applied across polarization ports. Thus, the antenna-port-domain beam vector is written as

$$\mathbf{c}_q(a,b) = \frac{1}{\sqrt{P_q}} \mathbf{1}_{P_q} \otimes \widetilde{\mathbf{c}}_q(a,b), \tag{43}$$

where P_q is the number of polarization ports and $\mathbf{c}_q(a,b) \in \mathbb{C}^{N_q}$ with $N_q = P_q N_q^{\mathrm{H}} N_q^{\mathrm{V}}$.

For compact indexing, the beam corresponding to (a,b) is mapped to a single index

$$\zeta_q(a,b) = (a-1)N_q^{\mathrm{H}} + b, \ \zeta_q = 1, \dots, N_q^{\mathrm{beam}}. \tag{44}$$

The BS DL codebook and UE uplink (UL) codebook are then respectively defined as

$$\mathscr{F}_{\mathrm{DL}} = \left\{\mathbf{f}_{\mathrm{DFT}}^{(1)}, \dots, \mathbf{f}_{\mathrm{DFT}}^{(N_{\mathrm{BS}}^{\mathrm{beam}})}\right\}, \ \mathbf{f}_{\mathrm{DFT}}^{(\zeta_{\mathrm{BS}})} = \mathbf{c}_{\mathrm{BS}}(a,b), \tag{45}$$

$$\mathscr{W}_{\mathrm{UL}} = \left\{\mathbf{w}_{\mathrm{DFT}}^{(1)}, \dots, \mathbf{w}_{\mathrm{DFT}}^{(N_{\mathrm{UE}}^{\mathrm{beam}})}\right\}, \ \mathbf{w}_{\mathrm{DFT}}^{(\zeta_{\mathrm{UE}})} = \mathbf{c}_{\mathrm{UE}}(a,b). \tag{46}$$

Here, $\mathscr{F}_{\mathrm{DL}}$ is used for BS-side DL analog precoding, whereas $\mathscr{W}_{\mathrm{UL}}$ is used for UE-side UL SRS precoding or receive beam selection. This notation separates the total number of antenna ports, N_{BS} and N_{UE}, from the number of spatial beams, $N_{\mathrm{BS}}^{\mathrm{beam}}$ and $N_{\mathrm{UE}}^{\mathrm{beam}}$.

2.9. SRS-based precoding and beam-pair selection

Following the generation of the per-link MIMO channel matrices $\mathbf{H}_{n,i}[k,t]$ in the previous subsection, the SRS-based beam selection stage operates on the effective channel between each BS–UE pair (n,i) at time t. For notation simplicity, we denote this instantaneous channel as

$$\mathbf{H}_t \triangleq \mathbf{H}_{n,i}[k_c,t],$$

where k_c represents the center subcarrier of the orthogonal frequency-division multiplexing band [27], and $\mathbf{H}_{t-\tau}$ is the channel at the previous transmission interval (used for SRS feedback). This convention allows compact expressions without loss of generality since the SLS simulator is able to track $\mathbf{H}_{n,i}[k,t]$ for all BS–UE links.

The analog DFT codebooks generated in the previous subsection are used in the SRS-based beam-pair selection process. Specifically, the UE selects an UL beam $\mathbf{w} \in \mathscr{W}_{\mathrm{UL}}$, while the BS selects a DL beam $\mathbf{f} \in \mathscr{F}_{\mathrm{DL}}$. The codebook sizes are $N_{\mathrm{UE}}^{\mathrm{beam}} = N_{\mathrm{UE}}^{\mathrm{H}} N_{\mathrm{UE}}^{\mathrm{V}}$ and $N_{\mathrm{BS}}^{\mathrm{beam}} = N_{\mathrm{BS}}^{\mathrm{H}} N_{\mathrm{BS}}^{\mathrm{V}}$, respectively. The SRS-based procedure then exploits these analog beams together with limited feedback to form a reciprocal beam-pair mapping between UL and DL.

- Step 1—UL Precoder Selection at the UE: Each UE selects its UL precoding vector $\mathbf{w}$ from the predefined UE-side DFT codebook $\mathscr{W}_{\mathrm{UL}} = \{\mathbf{w}_{\mathrm{DFT}}^{(1)}, \ldots, \mathbf{w}_{\mathrm{DFT}}^{(N_{\mathrm{UE}}^{\mathrm{beam}})}\}$ to maximize the projected channel gain based on the previous snapshot $\mathbf{H}_{t-\tau}$:

$$\mathbf{w} = \arg \max_{\mathbf{w}_i \in \mathscr{W}_{\mathrm{UL}}} \left\| \mathbf{w}_i^H \mathbf{H}_{t-\tau} \right\|^2. \tag{47}$$

- Step 2—UL SRS Transmission and Channel Estimation at the BS: The UE transmits a SRS using the selected analog beam $\mathbf{w}$. The BS correlates the received SRS against its receive codebook to estimate the effective precoded channel,

$$\hat{\mathbf{H}}_{t-\tau} = \mathbf{H}_{t-\tau} \mathbf{w}. \tag{48}$$

  In the proposed SLS platform, we assume perfect channel estimation (*i.e.*, $\hat{\mathbf{H}}_{t-\tau} = \mathbf{H}_{t-\tau}\mathbf{w}$), which isolates the effect of beam selection from estimation errors.

- Step 3—DL Beam Selection at the BS: Using the estimated UL channel, the BS exploits reciprocity to identify the optimal DL precoding beam $\mathbf{f}$ from its DFT-based codebook $\mathscr{F}_{\mathrm{DL}}$ that maximizes the received power at the UE:

$$\mathbf{f} = \arg \max_{\mathbf{f}_j \in \mathscr{F}_{\mathrm{DL}}} \left| \mathbf{w}^H \mathbf{H}_{t-\tau} \mathbf{f}_j \right|^2. \tag{49}$$

  Thus, the analog beam $\mathbf{f}$ selected at the BS is the one that provides the largest effective channel magnitude for the UE's chosen UL beam $\mathbf{w}$, forming a beam pair $(\mathbf{w}, \mathbf{f})$.

- Step 4—DL Transmission and Effective Channel: The BS transmits the DL data using the selected analog precoder $\mathbf{f}$ (possibly combined with a digital baseband precoder in later stages). The effective scalar channel between the BS and the UE during slot t is

$$h_{\mathrm{eff}}(t) = \mathbf{w}^H \mathbf{H}_t \mathbf{f}. \tag{50}$$

This equivalent channel gain incorporates both the spatial alignment achieved through the DFT codebooks and the temporal correlation of the time-varying channel. The pair $(\mathbf{w}, \mathbf{f})$ thus represents the best matched analog beams under the reciprocity assumption, and serves as the input to subsequent link adaptation and BLER prediction stages.

2.10. *Beamforming vector generation: MRC and IRC receivers*

After selecting the UL–DL beam pair $(\mathbf{w}, \mathbf{f})$ through the SRS-based procedure, the receiver combines multiple antenna signals to maximize the post-processing SINR. The proposed SLS platform implements two linear combining strategies: (i) MRC, which coherently aligns with the desired channel; and (ii) IRC, which additionally suppresses inter-cell and inter-user interference. Both are evaluated per link using the instantaneous channel snapshot $\mathbf{H}_t$.

2.10.1. Received signal model

For a given TTI and scheduled RB, the received baseband signal vector at UE i is modeled as

$$\mathbf{r}_t = \mathbf{H}_t \mathbf{f} s_t + \sum_{j \in \mathscr{I}_i(t)} \mathbf{H}_{t,j} \mathbf{f}_j s_{t,j} + \mathbf{n}_t, \tag{51}$$

where $\mathbf{H}_t$ is the desired MIMO channel between the serving BS and UE i, $\mathbf{f}$ is the selected DL precoder, and $\mathscr{I}_i(t)$ denotes the set of co-channel interfering transmissions affecting UE i at TTI t. The matrix $\mathbf{H}_{t,j}$ and vector $\mathbf{f}_j$ denote the corresponding channel and precoder of the jth interferer, respectively, while $\mathbf{n}_t \sim \mathscr{CN}(0, \sigma_n^2 \mathbf{I})$ is additive white Gaussian noise. The symbol s_t denotes the desired data symbol transmitted to UE i, whereas $s_{t,j}$ denotes the data symbol transmitted by the jth interfering BS or user. All transmitted symbols are assumed to be zero-mean, mutually independent, and normalized to unit average power, *i.e.*,

$$\mathbb{E}\{|s_t|^2\} = 1,\ \mathbb{E}\{|s_{t,j}|^2\} = 1,\ \mathbb{E}\{s_t s_{t,j}^*\} = 0,\ j \in \mathscr{I}_i(t). \tag{52}$$

The symbols are drawn from the normalized modulation constellation associated with the MCS selected by the link-adaptation module, such as QPSK, 16-QAM, 64-QAM, or 256-QAM. Since the receiver-side SINR is computed before link abstraction, the exact modulation order affects the BLER and TBS mapping in Section 2.11, but not the linear combining expressions in this subsection. The BS transmit power is accounted for through the effective received signal and interference powers used in the SINR and covariance computations.

2.10.2. Maximum Ratio Combining

The MRC (or matched-filter) receiver maximizes the coherent signal power by

$$\mathbf{w}_{\text{MRC}} = \frac{\mathbf{H}_t \mathbf{f}}{||\mathbf{H}_t \mathbf{f}||}. \tag{53}$$

This choice maximizes $|\mathbf{w}_{\text{MRC}}^H \mathbf{H}_t \mathbf{f}|^2$ under the assumption of spatially white noise and uncorrelated interference. The instantaneous post-combining SINR for MRC is

$$\gamma_{\text{MRC}}[t] = \frac{|\mathbf{w}_{\text{MRC}}^H \mathbf{H}_t \mathbf{f}|^2}{\mathbf{w}_{\text{MRC}}^H \mathbf{R}_{\eta,t} \mathbf{w}_{\text{MRC}}}, \tag{54}$$

where $\mathbf{R}_{\eta,t} = \mathbb{E}[(\mathbf{i}_t + \mathbf{n}_t)(\mathbf{i}_t + \mathbf{n}_t)^H]$ denotes the interference-plus-noise covariance matrix. In implementation, $\mathbf{R}_{\eta,t}$ is formed from the explicitly generated small-scale channels of the four dominant interfering BSs, while the residual interference from the remaining BSs is added as an average large-scale interference term. When $\mathbf{R}_{\eta,t} = \sigma_n^2 \mathbf{I}$, the expression reduces to $\gamma_{\text{MRC}} = \|\mathbf{H}_t \mathbf{f}\|^2 / \sigma_n^2$, making MRC optimal for noise-limited scenarios.

2.10.3. Interference rejection combining

When interference becomes dominant, the IRC receiver enhances robustness by whitening the interference-plus-noise covariance before combining. The IRC beamforming vector is

$$\mathbf{w}_{\text{IRC}} = \frac{\mathbf{R}_{\eta,t}^{-1} \mathbf{H}_t \mathbf{f}}{\|\mathbf{R}_{\eta,t}^{-1} \mathbf{H}_t \mathbf{f}\|}, \tag{55}$$

leading to the effective post-processing SINR

$$\gamma_{\text{IRC}}[t] = (\mathbf{H}_t \mathbf{f})^H \mathbf{R}_{\eta,t}^{-1} (\mathbf{H}_t \mathbf{f}). \tag{56}$$

The IRC receiver thus generalizes MRC and reduces to it when $\mathbf{R}_{\eta,t} = \sigma_n^2 \mathbf{I}$.

2.10.4. Integration in the SLS platform

Both combining vectors are updated at each TTI based on the instantaneous channel $\mathbf{H}_t$ and the estimated covariance $\mathbf{R}_{\eta,t}$. The corresponding effective channel gain used for SINR and throughput evaluation is

$$h_{\text{eff}}[t] = \mathbf{w}^H \mathbf{H}_t \mathbf{f}. \tag{57}$$

These methods enable the proposed SLS to evaluate receiver performance under both noise-limited and interference-limited conditions in ultra-dense network deployments.

2.11. Link adaptation and BLER prediction

The link adaptation module dynamically adjusts the modulation and coding scheme (MCS) based on the reported CQI from each UE. In the proposed SLS platform, an EESM–based approach is adopted to translate per–RB SINR values, derived from the effective channel output of MRC/IRC combining, into an equivalent link-level performance metric [28,29]. The overall process is summarized in Figure 4 and described as follows:

- Step 1—Effective SINR Computation: For each RB at TTI t, the instantaneous SINR of the UE, $\gamma_r[t]$, is derived from the effective channel $h_{\text{eff}}[t] = \mathbf{w}^H \mathbf{H}_t \mathbf{f}$ obtained in Equation (57). Depending on the receiver type, either $\gamma_{\text{MRC}}[t]$ or $\gamma_{\text{IRC}}[t]$ is used, as defined in Equations (54) and (56). The SINR, $\gamma_r[t]$, implicitly captures the joint influence of the analog precoder $\mathbf{f}$, receiver combiner $\mathbf{w}$, interference covariance $\mathbf{R}_\eta$, and noise power P_n.
- Step 2—EESM Aggregation: The EESM method converts the set of per–RB SINRs $\{\gamma_r[t]\}$ into a single equivalent SINR that represents the overall link quality:

$$\gamma_{\text{eff}}[t] = -\beta_m \ln\left(\frac{1}{N_{\text{RB}}}\sum_{r=1}^{N_{\text{RB}}} \exp\left(-\frac{\gamma_r[t]}{\beta_m}\right)\right), \tag{58}$$

where N_{RB} is the total number of RBs and β_m is the EESM calibration parameter associated with the selected MCS index m. In general, β_m depends on the modulation order and coding rate, and therefore different values may be used for QPSK, 16QAM, 64QAM, and 256QAM-based MCS levels.

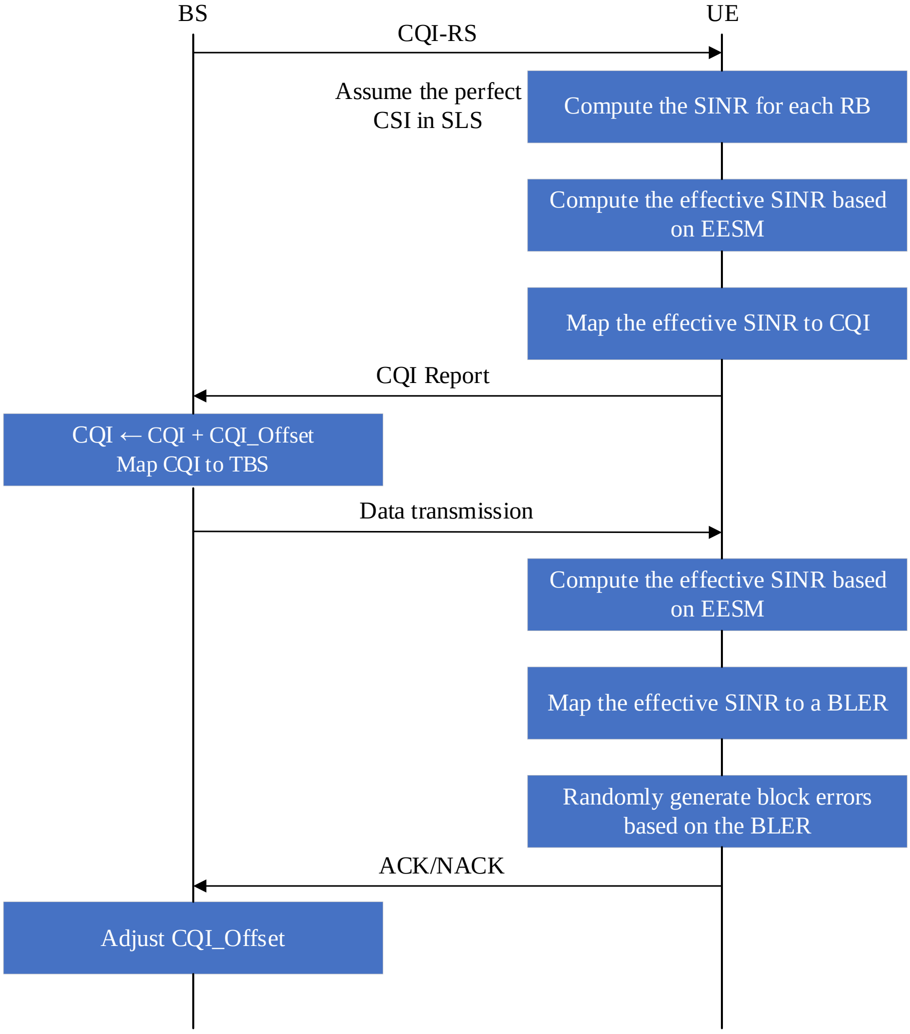

Figure 4. EESM-based link adaptation and BLER prediction chain in the proposed SLS platform.

In the present SLS implementation, a single effective calibration value $\beta_{\text{eff}} = 1.4$ is used for all active MCS levels. This value is treated as an aggregate EESM parameter calibrated over the MCS range activated in the InH_B scenario, rather than as an individually optimized value for each MCS. Equivalently, the implemented setting corresponds to

$$\beta_m \approx \beta_{\text{eff}} = 1.4, \ \forall m \in \mathscr{M}_{\text{act}}, \tag{59}$$

where $\mathscr{M}_{\text{act}}$ denotes the set of MCS levels selected during the simulation.
This simplification reduces the complexity of link abstraction and ensures that MRC and IRC receivers are compared under the same CQI, MCS, and BLER mapping procedure. Nevertheless,

because the optimal EESM parameter is MCS-dependent, the use of a single β_{eff} may introduce non-uniform BLER prediction accuracy across very low- and high-rate MCS levels. For example, cell-edge users operating at low MCS and cell-center users operating at high MCS may experience different levels of BLER fitting error. The impact of this approximation is partially mitigated by the fact that the proposed study focuses on relative receiver-level comparison under identical link abstraction settings. A per-MCS calibration table $\{\beta_m\}$ can be incorporated into the proposed framework without changing the remaining SLS modules.

- Step 3—CQI Mapping and Reporting: The UE converts the effective SINR $\gamma_{\text{eff}}[t]$ into a corresponding CQI index using a predefined mapping table, $\gamma_{\text{eff}} \to \text{CQI}$, defined for 5G NR MCS. CQI values are reported to the BS with a delay of τ TTIs. To mitigate channel aging, the BS may apply a correction offset $\text{CQI}_{\text{adj}} = \text{CQI} + \Delta_{\text{CQI}}$.
- Step 4—MCS and Transport Block Size (TBS) Selection: At the BS, the adjusted CQI determines the selected MCS level and the corresponding TBS for DL transmission:

$$\text{TBS} = f_{\text{TBS}}(\text{CQI}_{\text{adj}}, N_{\text{RB}}), \tag{60}$$

  where $f_{\text{TBS}}(\cdot)$ follows the 3GPP NR lookup tables [30].
- Step 5—BLER Estimation and ACK/NACK Generation: At the receiver, the BLER corresponding to γ_{eff} is estimated using an exponential model calibrated from link-level results:

$$\text{BLER}(\gamma_{\text{eff}}) = \frac{1}{2}\exp\left(-\frac{\gamma_{\text{eff}} - \gamma_0}{\kappa}\right), \tag{61}$$

  where γ_0 and κ are model parameters obtained from empirical fitting. Block errors are generated probabilistically according to this BLER, and acknowledgment (ACK)/negative acknowledgment (NACK) feedback is returned to complete the hybrid automatic repeat request loop [31].

This EESM-based link adaptation framework maintains consistency with the physical-layer channel model and combining procedures described in the previous subsections, providing realistic estimation of CQI, BLER, and throughput in ultra-dense 5G deployments while remaining computationally efficient for large-scale simulations.

2.12. *Computation of BLER and throughput*

Following link adaptation and EESM-based BLER prediction, the proposed SLS platform evaluates the actual BLER and user throughput through Monte Carlo–based random testing. For each transmitted transport block, a uniformly distributed random variable $u_{\text{rand}} \sim \mathscr{U}(0,1)$ is generated and compared with the predicted BLER value $\text{BLER}_{\text{EESM}}[t] = \text{BLER}(\gamma_{\text{eff}}[t])$ obtained from Equation (61). The transmission outcome is determined as

$$\begin{aligned} \text{if } u_{\text{rand}} > \text{BLER}_{\text{EESM}}[t] : N_s \leftarrow N_s + 1, \\ \text{else} : N_c \leftarrow N_c + 1, \end{aligned} \tag{62}$$

where N_s and N_c denote the numbers of successfully decoded and failed transport blocks, respectively.

The empirical BLER is computed as

$$\mathrm{BLER}_{\mathrm{sim}} = \frac{N_c}{N_s + N_c}, \tag{63}$$

representing the observed ratio of failed TBs over all transmitted ones.

2.12.1. User throughput

The instantaneous user throughput is then obtained as the sum of successfully received TBS normalized by the total simulation time:

$$T_k = \frac{\sum_{t=1}^{T_{\mathrm{sim}}} \mathrm{TBS}_{k,t} \cdot (1 - e_{k,t})}{T_{\mathrm{sim}} T_{\mathrm{TTI}}}, \tag{64}$$

where $e_{k,t} \in \{0,1\}$ indicates block failure for UE k at time t ($e_{k,t} = 1$ if the transmission fails), T_{sim} is the total number of simulated TTIs, and T_{TTI} denotes the TTI duration. The variable $\mathrm{TBS}_{k,t}$ is determined per-UE from the MCS level selected in Step 4 of link adaptation.

2.12.2. Cell throughput and spectral efficiency

The aggregate cell throughput is computed as the sum of all active UE throughputs,

$$T_{\mathrm{cell}} = \sum_{k=1}^{N_{\mathrm{UE}}} T_k, \tag{65}$$

and the average per-user throughput is $T_{\mathrm{avg,UE}} = T_{\mathrm{cell}}/N_{\mathrm{UE}}$. The corresponding average SE is defined as

$$\mathrm{SE}_{\mathrm{avg}} = \frac{T_{\mathrm{cell}}}{B}, \tag{66}$$

where B is the total system bandwidth. These metrics serve as key performance indicators (KPIs) for evaluating the throughput, capacity, and spectral utilization efficiency of the proposed ultra-dense network under both perfect and imperfect CSI conditions. The computed BLER, throughput, and spectral efficiency values form the basis of the system-level performance evaluation presented in Section 3, where SINR distributions, throughput CDFs, and CSI-error impacts for MRC and IRC receivers are analyzed.

3. Simulation environment and parameter configuration

To ensure comparability with standard 5G NR evaluations, the simulation parameters largely follow the assumptions in [32], and the InH_B configuration defined in [20]. Tables 1 and 2 summarize the key parameters used in the proposed SLS platform. The fixed value $\beta_{\mathrm{eff}} = 1.4$ is used consistently for all receiver configurations; therefore, although absolute BLER values may contain MCS-dependent fitting errors, the relative comparison between MRC and IRC is performed under identical link-abstraction assumptions. These assumptions define the baseline environment for all subsequent evaluations, including SINR distribution, BLER prediction, and throughput analysis. To improve the interpretability of the CDF-based simulation results, the curves are compared using three main criteria. First, a rightward shift of the CDF indicates an improvement in SINR or spectral efficiency. Second, the median point of the CDF is used to characterize the typical-user performance. Third, the 5th-percentile point is used to characterize cell-edge performance, which is particularly important in ultra-dense interference-limited deployments. For throughput-related comparisons, the CDF observations are further supported by the numerical indicators in Tables 3 and 4, including average cell throughput, average UE throughput, average UE SE, 5% UE throughput, 5% UE SE, and area throughput.

Table 1. General simulation parameters.

Parameter	Values
Carrier frequency (f_c)	30 GHz
System bandwidth (B)	50 MHz
No. of RBs N_{RB}	66
Network layout	InH_B
Number of cells	12
Number of UEs per cell	10
BS antenna height (h_{BS})	3 m
UE antenna height (h_{UE})	1.5 m
BS transmit power ($P_{\mathrm{BS},n}$)	23 dBm
BS antenna gain (G_n)	5 dBi
UE antenna gain (G_i)	5 dBi
Noise figure (BS/UE)	5/9 dB
Thermal noise level	-174 dBm/Hz
No. of BS antenna ports N_{BS}	64
No. of UE antenna ports N_{UE}	32
$(N^{\mathrm{H}}_{\mathrm{BS,el}}, N^{\mathrm{V}}_{\mathrm{BS,el}}, N^{\mathrm{H}}_{\mathrm{BS,pan}}, N^{\mathrm{V}}_{\mathrm{BS,pan}}, P_{\mathrm{BS}})$	$(8,4,1,1,2)$
$(N^{\mathrm{H}}_{\mathrm{UE,el}}, N^{\mathrm{V}}_{\mathrm{UE,el}}, N^{\mathrm{H}}_{\mathrm{UE,pan}}, N^{\mathrm{V}}_{\mathrm{UE,pan}}, P_{\mathrm{UE}})$	$(4,2,2,1,2)$
BS spatial dimensions $(N^{\mathrm{H}}_{\mathrm{BS}}, N^{\mathrm{V}}_{\mathrm{BS}})$	$(8,4)$
UE spatial dimensions $(N^{\mathrm{H}}_{\mathrm{UE}}, N^{\mathrm{V}}_{\mathrm{UE}})$	$(8,2)$
Number of sub-rays each cluster (N_ℓ)	20
No. of clusters (L)	19
Transmission time interval (T_{TTI})	1 ms
Delay (τ)	20 TTIs
EESM calibration parameter	$\beta_{\mathrm{eff}} = 1.4$
BLER model parameters (γ_0, κ)	(1.2 dB, 1.5)
UE speed	3 km/h
CSI error	$\sigma_{\mathrm{CSI}} \in [0, 0.2]$

Table 2. Channel and scheduler configuration.

Parameter	Values
Channel model	Indoor Hotspot
Traffic model	Full buffer
Subcarrier spacing	60 kHz
Scheduler	Round-Robin
Scheduling delay	5 ms
Inter-cell interference modeling	Full small-scale MIMO channels for four strongest large-scale interferers; average large-scale residual interference for others
Path-loss exponent ($n^{\mathrm{InH\_B}}$)	1.73 (LoS), 2.36 (NLoS) [20]
Shadow fading std. dev. ($\sigma^{\mathrm{InH\_B}}$)	3.0 dB (LoS), 8.0 dB (NLoS)
NLoS offset ($\Delta^{\mathrm{InH\_B}}_{\mathrm{NLoS}}$)	17.0 dB
Cross-polarization ratio	$\mathcal{N}(9, 3^2)$ dB
Rician K-factor (K_{dB})	$\mathcal{N}(9, 5^2)$ dB
Angular spreads (σ_{ASD}, σ_{ASA}, σ_{ZSD}, σ_{ZSA})	(17°, 22°, 3°, 7°)

Table 3. Performance summary of the proposed SLS platform under perfect CSI conditions (InH_B scenario).

Parameters	MRC receiver	IRC receiver	Phase 2 calibration average
Average cell throughput (Mbps)	152.98	192.03	140.37
Average UE throughput (Mbps)	15.30	19.20	14.04
Average UE SE (bps/Hz)	0.38	0.48	0.35
5% UE throughput (Mbps)	4.4	7.6	6.8
5% UE SE (bps/Hz)	0.11	0.19	0.17
Average throughput per area (Mbps/m^2)	0.3060	0.3841	0.2807

Table 4. Summary of system-level results with CSI errors.

Parameters	Proposed MRC receiver	Proposed IRC receiver
Average cell throughput (Mbps)	83.22	117.94
Average UE throughput (Mbps)	8.32	11.79
Average UE SE (bps/Hz)	0.21	0.29
5% UE throughput (Mbps)	1.2	3.2
5% UE SE (bps/Hz)	0.03	0.08
Average throughput per area (Mbps/m^2)	0.1664	0.2359

Figure 5 illustrates the outcome of the UE dropping and BS association procedure in the proposed SLS framework for the InH_B scenario. Each square marker represents a BS, while circular markers denote UEs randomly distributed over a 120 m $\times$ 50 m floor area. The color of each UE corresponds to the received RSRP, where warmer colors indicate stronger signal levels. The association process follows the maximum-RSRP criterion defined in [20], in which each UE is connected to the BS providing the highest large-scale received power. As observed, users located near cell boundaries experience weaker RSRP values (blue-to-cyan color range), while those closer to BSs achieve stronger links (red-to-yellow tones). The resulting UE–BS association confirms that the proposed initialization phase correctly implements spatial user deployment, distance-based path-loss, and probabilistic LoS modeling consistent with standardized InH_B channel definitions.

To validate the developed SLS platform, the SINR CDF is compared with the reference results reported by multiple vendors in [32] for the InH_B scenario. As shown in Figure 6, the proposed simulator closely reproduces the statistical behavior of SINR observed in commercial-grade system-level tools used by ZTE, Ericsson, Huawei, Nokia, Qualcomm, and others. The results confirm that the proposed SLS implementation accurately follows the standardized channel, antenna, and interference modeling defined in [20] and [21]. The median SINR obtained from the proposed framework differs by less than 2 dB from the reference models, ensuring the reliability of subsequent performance evaluations. The close match between the proposed SINR CDF and the 3GPP Phase-2 calibration curves also indicates that the dominant-interferer approximation preserves the aggregate interference statistics sufficiently well for system-level performance evaluation.

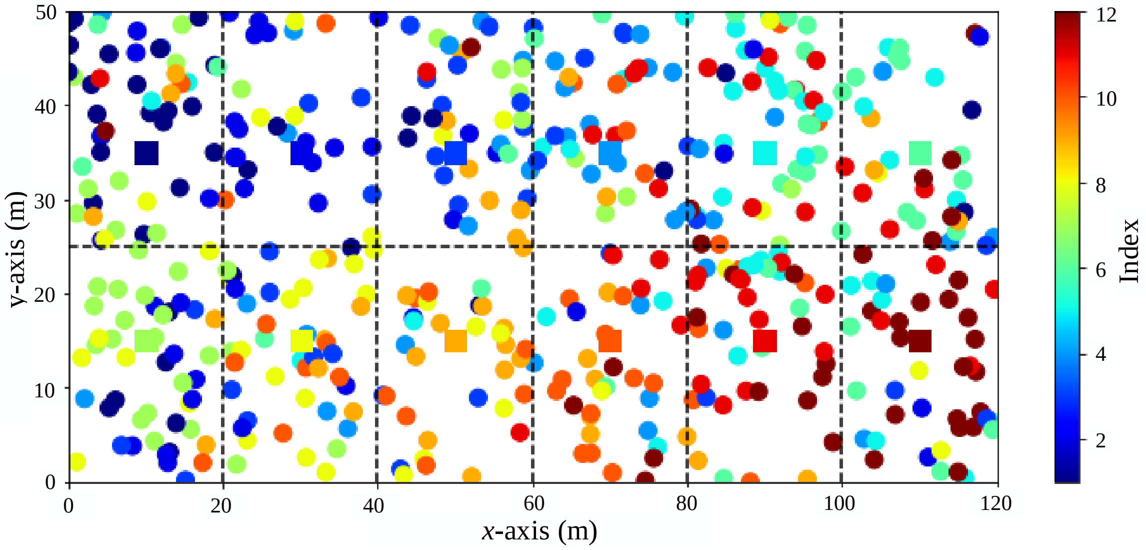

Figure 5. Spatial distribution of UEs and BSs in the InH_B scenario. Squares represent BSs, circles represent UEs, and the color map indicates the received signal power used for UE–BS association.

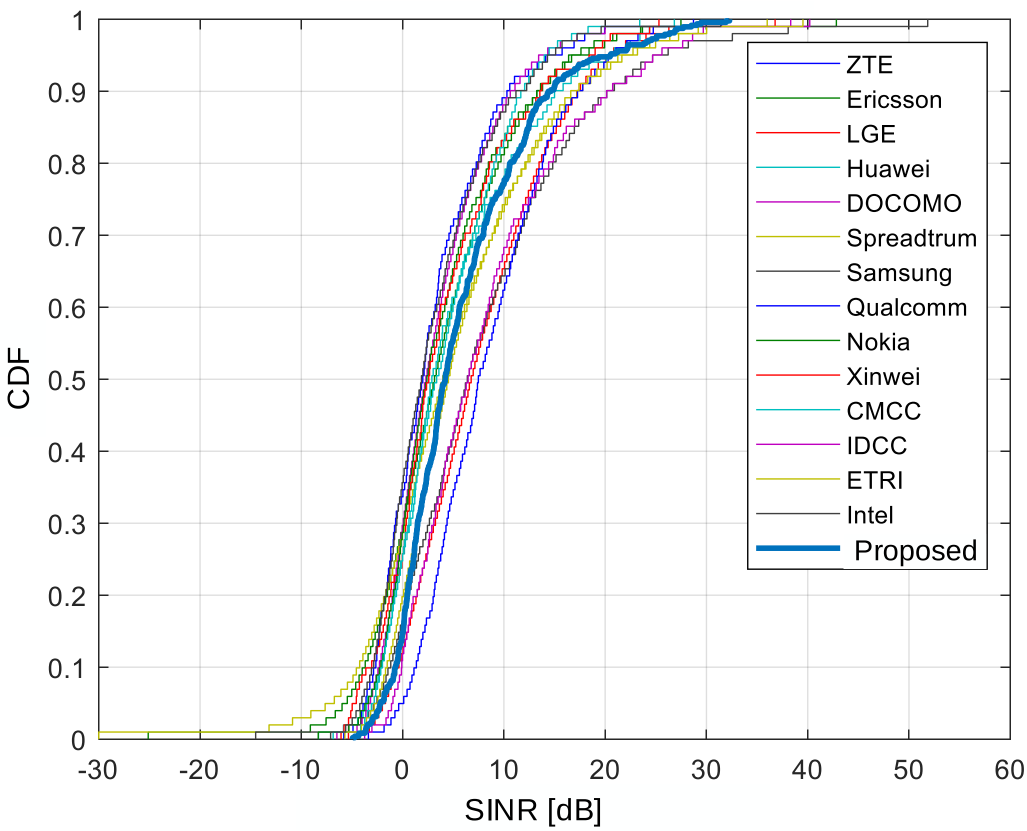

Figure 6. Validation of the proposed SLS platform: CDF of SINR in the InH_B scenario compared with reference simulation results from 3GPP calibration participants [32]. The comparison is interpreted in terms of CDF alignment, median SINR deviation, and overall distribution consistency.

To further benchmark the receiver performance, Figure 7 illustrates the CDF of user SE for the MRC receiver under perfect CSI conditions. In this configuration, both the transmitter and receiver are assumed to have full knowledge of the CSI, thereby eliminating estimation and quantization errors. In these CDF plots, the median SE is used as a typical-user indicator, while the 5th-percentile SE is used as a cell-edge indicator. A rightward shift of the CDF therefore indicates improved spectral efficiency over a broad range of users. The proposed architecture yields SE statistics that closely match those reported by major 3GPP calibration participants. Compared with the corresponding MRC case under imperfect CSI, the SE distribution shifts rightward by approximately 0.1 bps/Hz at the median and achieves up to 20% gain in the lower 5%-tile region. Although MRC does not actively suppress inter-cell interference, the improvement demonstrates the importance of accurate CSI for coherent signal combining and reliable power aggregation in dense indoor deployments. Overall, the results confirm that the implemented SLS framework and receiver modules of the proposed architecture produce consistent behavior with standardized 3GPP benchmarks, validating its suitability for evaluating advanced channel-aware algorithms in future work.

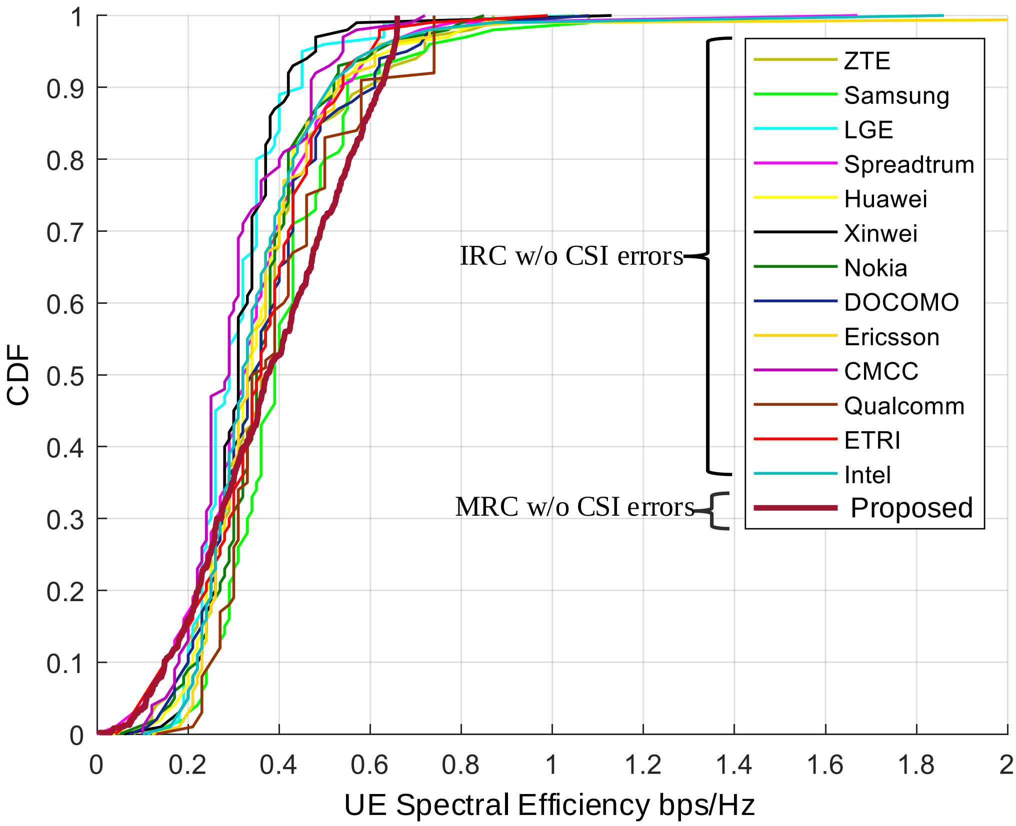

Figure 7. CDF of user spectral efficiency in the InH_B scenario for the proposed architecture using an MRC receiver with perfect CSI, compared with reference 3GPP calibration results. The CDF is interpreted using the rightward curve shift, median SE, and 5th-percentile SE as comparison criteria.

To establish a performance upper bound, Figure 8 shows the CDF of the user SE for the IRC receiver under perfect CSI conditions. In this case, the CSI is assumed to be fully known at both transmitter and receiver, eliminating estimation and feedback errors. The proposed SLS framework again aligns well with the 3GPP calibration results from industrial participants, demonstrating high consistency across the entire CDF range.

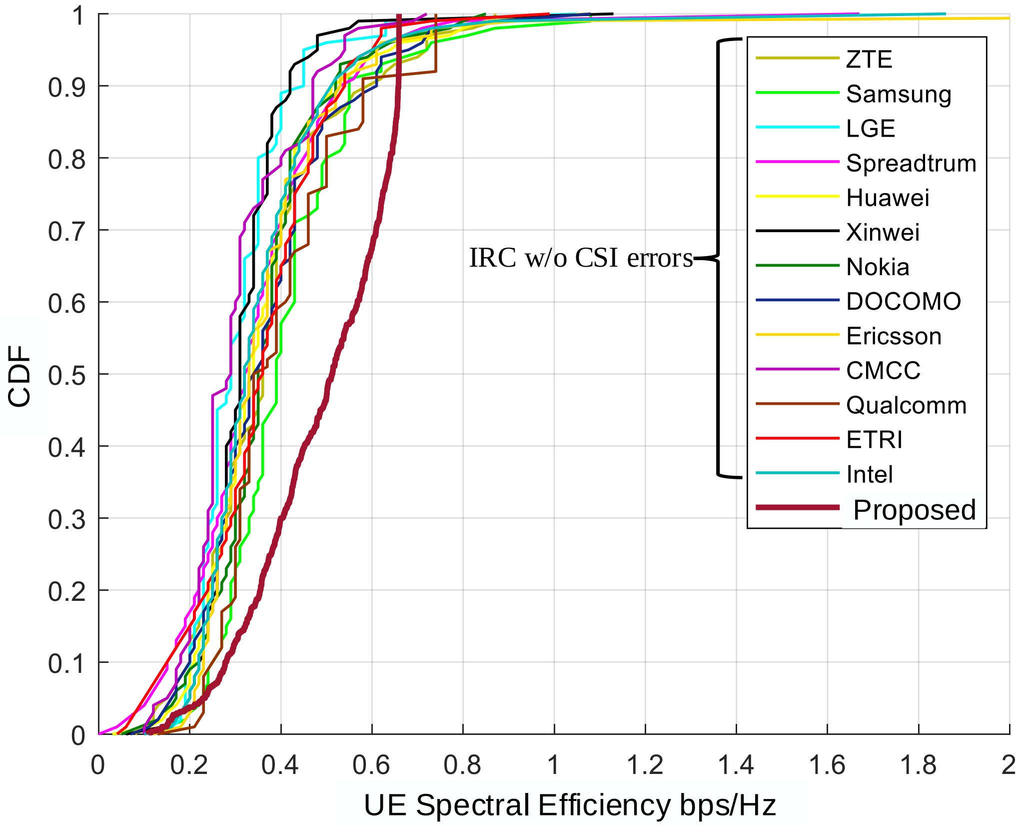

Figure 8. CDF of user spectral efficiency in the InH_B scenario for the IRC receiver with perfect CSI, compared with reference 3GPP calibration results. The median and 5th-percentile SE are used to assess typical-user and cell-edge performance, respectively.

Compared with the imperfect-CSI case in Figure 6, the median SE improves by approximately 0.1–0.2 bps/Hz, and the 5%-tile SE shows a noticeable gain of nearly 25%. This improvement originates from accurate interference covariance estimation in the IRC filter, enabling more effective suppression of inter-cell interference. The close overlap between the proposed model and the reference curves (e.g., from Nokia, Ericsson, and Huawei) confirms the correctness of the implemented interference modeling and receiver architecture.

Table 3 summarizes the key performance metrics obtained from the proposed SLS platform under perfect CSI conditions. The results indicate that the IRC receiver consistently outperforms the MRC receiver in all measured indicators. Compared with the 3GPP Phase 2 calibration average, the proposed simulator achieves 9%–15% higher average cell throughput and comparable 5%-tile user throughput. The alignment between the proposed and reference results confirms that the implemented InH_B channel, receiver, and scheduling modules accurately reproduce standardized system-level performance trends.

In practical systems, the CSI obtained at the BS and UE is imperfect due to estimation errors, quantization, and feedback delays. To avoid ambiguity, we use the normalized mean-squared error (NMSE) as the primary CSI uncertainty metric throughout this paper. The imperfect CSI at time t is modeled as

$$\hat{\mathbf{H}}_t = \mathbf{H}_t + \sigma_{\mathrm{CSI}}\mathbf{E}_t, \tag{67}$$

where $\mathbf{H}_t$ is the true instantaneous channel matrix, and $\mathbf{E}_t$ is an independent random error matrix normalized such that $\mathbb{E}\{\|\mathbf{E}_t\|_F^2\} = \mathbb{E}\{\|\mathbf{H}_t\|_F^2\}$. The CSI uncertainty level is then measured by

$$\mathrm{NMSE}_{\mathrm{CSI}} = \frac{\mathbb{E}\big[\|\hat{\mathbf{H}}_t - \mathbf{H}_t\|_F^2\big]}{\mathbb{E}\big[\|\mathbf{H}_t\|_F^2\big]} = \sigma_{\mathrm{CSI}}^2. \tag{68}$$

Under this normalization, the equivalent channel correlation coefficient between the true and estimated channels is

$$\rho_{\mathrm{CSI}} = \frac{\mathbb{E}\big[\langle \mathbf{H}_t, \hat{\mathbf{H}}_t\rangle_F\big]}{\sqrt{\mathbb{E}\{\|\mathbf{H}_t\|_F^2\}\mathbb{E}\{\|\hat{\mathbf{H}}_t\|_F^2\}}} = \frac{1}{\sqrt{1+\sigma_{\mathrm{CSI}}^2}}, \tag{69}$$

where $\langle \mathbf{A}, \mathbf{B}\rangle_F = \mathrm{tr}(\mathbf{A}^H\mathbf{B})$ denotes the Frobenius inner product. Thus, ρ_{CSI} is not treated as an independent parameter, but as an equivalent representation of the same CSI uncertainty level. During simulation, σ_{CSI} is varied between 0 and 0.2, where $\sigma_{\mathrm{CSI}} = 0$ corresponds to perfect CSI. All precoder selections and SINR evaluations are performed using $\hat{\mathbf{H}}_t$ when imperfect CSI is considered.

Figure 9 depicts the CDF of user SE for the proposed SLS architecture using the MRC receiver under imperfect CSI conditions. In this case, the estimated channel is generated according to Equation (67) with $\sigma_{\mathrm{CSI}} > 0$, corresponding to $\mathrm{NMSE}_{\mathrm{CSI}} = \sigma_{\mathrm{CSI}}^2$. Equivalently, the associated channel correlation coefficient is given by Equation (69), and is therefore not an independent simulation parameter. As shown in the figure, the spectral efficiency of the MRC receiver degrades noticeably compared to the perfect-CSI case due to non-coherent signal combining and residual interference. At the median, the SE drops from approximately 0.38 bps/Hz to 0.32 bps/Hz, while the 5%-tile users experience up to a 25% reduction, illustrating the high sensitivity of MRC to CSI mismatch. Despite this degradation, the proposed SLS results remain consistent with 3GPP Phase 2 calibration datasets, such as those reported by Nokia, Ericsson, and Huawei, validating the correct implementation of the CSI error model and MRC receiver within the developed framework.

Figure 10 illustrates the CDF of user SE for the proposed SLS architecture when the IRC receiver operates under imperfect CSI conditions. The CSI inaccuracy is modeled using the same NMSE-based error formulation in Equations (67)–(68). As σ_{CSI}^2 increases, the equivalent correlation coefficient ρ_{CSI} in Equation (69) decreases, reducing the accuracy of interference covariance estimation and beamforming weights. As shown in the figure, CSI errors lead to a noticeable degradation in SE compared with the perfect-CSI case; however, the IRC receiver still provides significant gains over MRC under the same error levels. At the 50%-tile, the SE achieved by the proposed IRC receiver is approximately 0.44 bps/Hz, maintaining about 15% improvement relative to the MRC counterpart with identical CSI quality. The tail region (5% UE percentile) also remains robust, confirming the inherent interference-suppression capability of the IRC algorithm even with partially inaccurate channel information. The results demonstrate that the proposed SLS framework accurately reproduces the degradation trend reported in the 3GPP calibration datasets, with the proposed architecture's curve lying between vendor baselines such as Huawei, Nokia, and Qualcomm. This consistency validates the reliability of the CSI error modeling and the correctness of the implemented IRC receiver for evaluating realistic dense indoor deployments.

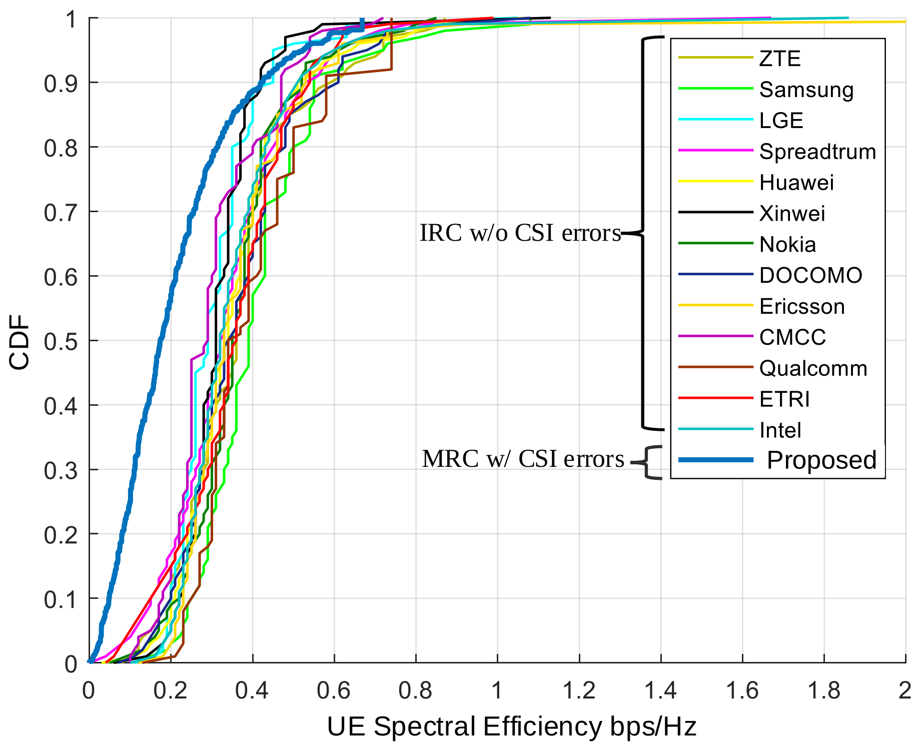

Figure 9. CDF of user spectral efficiency in the InH_B scenario for the proposed architecture using an MRC receiver under imperfect CSI conditions. The degradation is assessed by comparing the CDF shift, median SE, and 5th-percentile SE with the perfect-CSI reference.

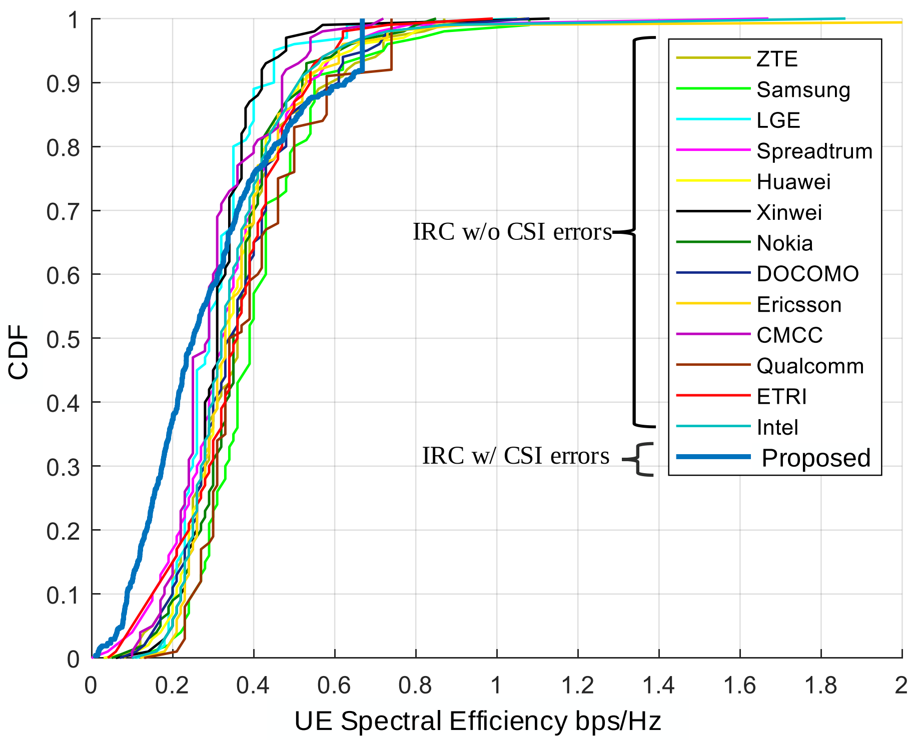

Figure 10. CDF of user spectral efficiency in the InH_B scenario for the proposed architecture using an IRC receiver under imperfect CSI conditions. The figure highlights receiver robustness using median SE and 5th-percentile SE under identical CSI-error conditions.

Table 4 summarizes the SLS results of the proposed framework in the 3GPP InH_B scenario when CSI imperfections are considered. Both the MRC and IRC receivers were evaluated under identical CSI error conditions. As shown in the table, the IRC receiver consistently outperforms the MRC receiver across all performance metrics. The average cell throughput increases from 83.22 Mbps to 117.94 Mbps, corresponding to an improvement of approximately 41.7%. Similarly, the average user throughput rises from 8.32 Mbps to 11.79 Mbps, while the average SE improves from 0.21 bps/Hz to 0.29 bps/Hz. The 5% user throughput, a key indicator for cell-edge users, shows a notable gain, more than doubling from 1.2 Mbps (MRC) to 3.2 Mbps (IRC), which highlights the IRC receiver's superior interference suppression capability. In terms of area throughput, the IRC receiver achieves 0.2359 Mbps/m^2, representing a 42% gain compared with MRC. Overall, these results demonstrate that the proposed IRC architecture maintains strong robustness under CSI inaccuracies and effectively mitigates inter-cell interference, whereas MRC suffers more severe degradation due to its non-interference-aware nature.

Although the proposed framework provides a realistic and modular SLS environment, several practical challenges may arise when extending it toward real-world deployment or hardware-in-the-loop validation. First, accurate CSI acquisition is difficult in dense indoor networks because SRS feedback, channel estimation, and beam-pair selection are affected by feedback delay, quantization, mobility, and hardware calibration errors. Second, the real-time implementation of IRC requires reliable estimation of the interference-plus-noise covariance matrix, which may increase computational complexity and signaling overhead compared with MRC. Third, although the dominant-interferer approximation reduces simulation complexity, real deployments may exhibit time-varying interference patterns, especially under dynamic traffic loads and user mobility. Fourth, the EESM-based link abstraction requires careful calibration across different MCS levels; using an aggregate calibration parameter may simplify the simulator but can introduce non-uniform BLER prediction accuracy for cell-edge and cell-center users. Finally, practical antenna arrays may suffer from finite phase-shifter resolution, RF-chain impairments, mutual coupling, synchronization errors, and implementation losses that are not fully captured by ideal DFT codebooks. These issues do not invalidate the proposed SLS framework, but they indicate important directions for future extensions, including measurement-based calibration, per-MCS EESM fitting, hardware-aware beamforming, and real-time validation.

4. Conclusion

This paper presented a unified SLS framework for realistic evaluation of 5G NR MIMO networks in the InH_B scenario. The proposed model integrates standardized 3GPP channel modeling, DFT-based analog beamforming, SRS-assisted beam-pair selection, and EESM-based link adaptation within a modular and computationally efficient environment. By jointly modeling large-scale and small-scale effects, the framework provides accurate prediction of end-to-end performance under both perfect and imperfect CSI conditions. Simulation results show strong agreement with the 3GPP Phase 2 calibration datasets, validating the correctness of the implementation. Under CSI uncertainty, the IRC receiver demonstrated substantial robustness, achieving up to 42% higher average cell throughput and more than 160% gain at the 5th-percentile UE throughput compared to the MRC baseline. These results highlight the importance of interference-aware combining in dense multi-cell environments. Overall, the developed SLS framework offers a reliable and extensible reference for evaluating MIMO receiver algorithms, hybrid beamforming, and machine-learning-assisted link adaptation toward beyond-5G and 6G wireless systems.

Data availability statement

No supplementary or additional data were generated in this study.

Declaration of generative AI and AI-assisted technologies

During the preparation of this manuscript, the authors used ChatGPT 5.5 by OpenAI only for language editing, grammar checking, and readability improvement. All technical content, simulation models, numerical results, analyses, interpretations, and conclusions were developed and verified by the authors. The authors reviewed and edited the manuscript and take full responsibility for its content.

Acknowledgments

The authors acknowledge the research facilities and academic environment provided by Phenikaa University. This research received no external funding.

Authors' contribution

Conceptualization, T.V.L. and N.C.L.; methodology, T.V.L.; software, T.V.L. and N.V.D.; validation, T.V.L., N.V.D. and N.T.N.; data curation, N.V.D.; writing—original draft preparation, T.V.L.; writing—review and editing, T.V.L., N.V.D., N.T.N. and N.C.L.; visualization, N.T.N.; supervision, N.C.L.; project administration, N.C.L. All authors have read and agreed to the published version of the manuscript.

Conflicts of interest

Nguyen Cong Luong holds the position of Editorial Board Member for *Advanced Information and Communication* and has not peer reviewed or made any editorial decisions for this paper. The authors declare no other conflicts of interest.

References

[1] Anand A, de Veciana G, Shakkottai S. Joint scheduling of URLLC and eMBB traffic in 5G wireless networks. *IEEE/ACM Trans. Networking* 2020, 28(2):477–490.

[2] D'Oro S, Bonati L, Restuccia F, Melodia T. Coordinated 5G network slicing: how constructive interference can boost network throughput. *IEEE/ACM Trans. Networking* 2021, 29(4):1881–1894.

[3] Soldani D, Guo YJ, Barani B, Mogensen P, I CL, *et al.* 5G for ultra-reliable low-latency communications. *IEEE Network* 2018, 32(2):6–7.

[4] Ge X, Tu S, Mao G, Wang C, Han T. 5G ultra-dense cellular networks. *IEEE Wireless Commun.* 2016, 23(1):72–79.

[5] Duong TQ, Chu X, Suraweera HA. *Ultra-Dense Networks for 5G and Beyond: Modelling, Analysis, and Applications*, 1st ed. Hoboken: John Wiley & Sons, 2019.

[6] Narasimha D, Shakkottai S, Ying L. Age-dependent distributed MAC for ultra-dense wireless networks. *IEEE/ACM Trans. Networking* 2023, 31(4):1674–1687.

[7] Narasimha D, Shakkottai S, Ying L. A mean field game analysis of distributed MAC in ultra-dense multichannel wireless networks. *IEEE/ACM Trans. Networking* 2020, 28(5):1939–1952.

[8] Wang X, Chen Y, Mai Z. A novel design of system level simulator for heterogeneous networks. In *Proceedings of 2017 IEEE Globecom Workshops (GC Wkshps)*, Singapore, December 4–8, 2017, pp. 1–6.

[9] Hao L, Fastenbauer A, Schwarz S, Rupp M. Towards system level simulation of reconfigurable intelligent surfaces. In *Proceedings of 2022 International Symposium ELMAR*, Zadar, Croatia, September 12–14, 2022, pp. 81–84.

[10] Li L, Shao W, Zhou X. A flexible scheduling algorithm for the 5th-generation networks. *Intell. Converged Networks* 2021, 2(2):101–107.

[11] Shah SSA. CSI data between Alice and Bob using Vienna Simulator 5G. 2025. Available: https://doi.org/10.21227/6e31-zj53 (accessed on 15 August 2026).

[12] Gupta M, Roberts IP, Andrews JG. System-level analysis of full-duplex self-backhauled millimeter wave networks. *IEEE Trans. Wireless Commun.* 2023, 22(2):1130–1144.

[13] Madapatha C, Makki B, Fang C, Teyeb O, Dahlman E, *et al.* On integrated access and backhaul networks: current status and potentials. *IEEE Open J. Commun. Soc.* 2020, 1:1374–1389.

[14] Polese M, Giordani M, Zugno T, Roy A, Goyal S, *et al.* Integrated access and backhaul in 5G mmWave networks: potential and challenges. *IEEE Commun. Mag.* 2020, 58(3):62–68.

[15] Dai L, Gao X, Wang Z. Energy-efficient hybrid precoding based on successive interference cancelation for millimeter-wave massive MIMO systems. In *Proceedings of 2015 Radio and Antenna Days of the Indian Ocean (RADIO)*, Belle Mare, Mauritius, September 21–24, 2015, pp. 1–2.

[16] Xu Q, Sun J, Xu Z. Robust frequency selective precoding for downlink massive MIMO in 5G broadband system. *IEEE Trans. Veh. Technol.* 2023, 72(12):15941–15952.

[17] Lai X, Wu T, Yao J, Pan C, Elkashlan M, *et al.* On performance of fluid antenna system using maximum ratio combining. *IEEE Commun. Lett.* 2024, 28(2):402–406.

[18] Sibbett T, Moradi H, Boroujeny B. Normalized matched filter for blind interference suppression in filter bank multicarrier spread spectrum systems. *IEEE Access* 2022, 10:64270–64282.

[19] Léost Y, Abdi M, Richter R, Jeschke M. Interference rejection combining in LTE networks. *Bell Labs Tech. J.* 2012, 17(1):25–49.

[20] International Telecommunication Union. Guidelines for evaluation of radio interface technologies for IMT-2020. 2017. Available: https://www.itu.int/pub/R-REP-M.2412 (accessed on 15 August 2026).

[21] 3GPP. Study on channel model for frequencies from 0.5 to 100 GHz. 2026. Available: https://www.academia.edu/39972623/3_rd_Generation_Partnership_Project_Technical_Specification_Group_Radio_Access_Network_Study_on_channel_model_for_frequencies_from_0_5_to_100_GHz_Release_14 (accessed on 15 August 2026).

[22] Balharith T, Alhaidari F. Round Robin scheduling algorithm in CPU and cloud computing: a review. In *Proceedings of 2019 2nd International Conference on Computer Applications & Information Security (ICCAIS)*, Riyadh, Saudi Arabia, May 1–3, 2019, pp. 1–7.

[23] Van Le T, Lee K. Adaptive perturbation-aided opportunistic hybrid beamforming for mmWave systems. *IEEE Trans. Veh. Technol.* 2020, 69(6):6554–6562.

[24] Nor AM, Fratu O, Halunga S, Alyosef A, Zaharis ZD, *et al.* Demand based proportional fairness scheduling for 5G eMBB services. In *Proceedings of 2022 IEEE International Black Sea Conference on Communications and Networking (BlackSeaCom)*, Sofia, Bulgaria, June 6–9, 2022, pp. 263–268.

[25] Chang H, Sree R, Chen H, Zhang J, Liu L. MADRL based scheduling for 5G and beyond. In *Proceedings of MILCOM 2022–2022 IEEE Military Communications Conference (MILCOM)*, Rockville, USA, November 28–December 2, 2022, pp. 873–878.

[26] Shaban AW, Damen O, Xin Y, Au E. Statistically-aided codebook-based hybrid precoding for mmWave single-user MIMO systems. In *Proceedings of 2020 IEEE International Conference on Communications Workshops (ICC Workshops)*, Dublin, Ireland, June 7–11, 2020, pp. 1–6.

[27] Wang K. Design and performance analysis of OFDM systems in 5G networks. In *Proceedings of 2024 IEEE 2nd International Conference on Sensors, Electronics and Computer Engineering (ICSECE)*, Jinzhou, China, August 29–31, 2024, pp. 1840–1844.

[28] Song H, Kwan R, Zhang J. On the average output SNR of exponential effective SNR mapping over Nakagami-m fading channels. In *Proceedings of 2009 IEEE 70th Vehicular Technology Conference Fall*, Anchorage, USA, September 20–23, 2009, pp. 1–5.

[29] Liu H, Cai L, Yang H, Li D. EESM based link error prediction for adaptive MIMO-OFDM system. In *Proceedings of 2007 IEEE 65th Vehicular Technology Conference—VTC2007-Spring*, Dublin, Ireland, April 22–25, 2007, pp. 559–563.

[30] 3GPP. 5G NR physical layer procedures for data. 2026. Available: https://3gpp-explorer.com/spec/?specNumber=38214&release=Rel-18 (accessed on 15 August 2026).

[31] Tuninato R, Maiolini Capez G, Mazzali N, Garello R. 5G new radio for non-terrestrial networks: analysis and comparison of HARQ and RLC ARQ performance over satellite links. *IEEE Access* 2025, 13:75400–75415.

[32] ZTE, ZTE Microelectronics. Evaluation assumptions for phase 2 NR MIMO system-level calibration. Year. Available: https://www.3gpp.org/ftp/tsg_ran/WG1_RL1/TSGR1_88/Docs/R1-1701825.zip (accessed on 15 August 2026).